ModIs Dust AeroSol (MIDAS): A global fine resolution dust optical depth dataset

Antonis Gkikas[1], Emmanouil Proestakis[1], Vassilis Amiridis[1], Stelios Kazadzis[2,3], Enza Di Tomaso[4], Alexandra Tsekeri[1], Eleni Marinou[5], Nikos Hatzianastassiou[6] and Carlos Pérez García-Pando[4,7]

[1]Institute for Astronomy, Astrophysics, Space Applications and Remote Sensing, National Observatory of Athens, Athens, 15236, Greece

[2]Physikalisch-Meteorologisches Observatorium Davos, World Radiation Center, Switzerland

[3]Institute of Environmental Research and Sustainable Development, National Observatory of Athens, Greece

[4]Barcelona Supercomputing Center, Barcelona, Spain

[5]Deutsches Zentrum für Luft- und Raumfahrt (DLR), Institut für Physik der Atmosphäre, Oberpfaffenhofen, Germany

[6]Laboratory of Meteorology, Department of Physics, University of Ioannina, Ioannina, Greece

[7]ICREA, Catalan Institution for Research and Advanced Studies, Barcelona, Spain

Corresponding author: Antonis Gkikas (agkikas@noa.gr)

Abstract

Monitoring and describing the spatiotemporal variability of dust aerosols is crucial to understand their multiple effects, related feedbacks and impacts within the Earth system. This study describes the development of the MIDAS (ModIs Dust AeroSol) dataset. MIDAS provides columnar daily dust optical depth (DOD) at 550 nm at global scale and fine spatial resolution (0.1° x 0.1°) over a 15-year period (2003-2017). This new dataset combines quality filtered satellite aerosol optical depth (AOD) retrievals from MODIS-Aqua at swath level (Collection 6.1, Level 2), along with DOD-to-AOD ratios provided by MERRA-2 reanalysis to derive DOD on the MODIS native grid. The uncertainties of MODIS AOD and MERRA-2 dust fraction with respect to AERONET and LIVAS, respectively, are taken into account for the estimation of the total DOD uncertainty. MERRA-2 dust fractions are in very good agreement with those of LIVAS across the "dust belt", in the Tropical Atlantic Ocean and the Arabian Sea; the agreement degrades in North America and the Southern Hemisphere where dust sources are smaller. MIDAS, MERRA-2 and LIVAS DODs strongly agree when it comes to annual and seasonal spatial patterns, with collocated global DOD averages of 0.033, 0.031 and 0.029, respectively; however, deviations in dust loading are evident and regionally dependent. Overall, MIDAS is well correlated with AERONET-derived DODs (R=0.89), only showing a small positive bias (0.004 or 2.7%). Among the major dust areas of the planet, the highest R values (> 0.9) are found at sites of N. Africa, Middle East and Asia. MIDAS expands, complements and upgrades existing

observational capabilities of dust aerosols and it is suitable for dust climatological studies, model evaluation and data assimilation.

1. Introduction

Among tropospheric and stratospheric aerosol species, dust aerosol is the most abundant component in terms of mass, contributing more than half of the global aerosol amount (Textor et al., 2006; Zender et al., 2011). Preferential sources of dust aerosols are located in areas where precipitation is low, thus favoring aridity, whereas a significant contributing factor is the accumulation of alluvial sediments. Such regions comprise deserts, dry lake beds and ephemeral channels (e.g., Middleton and Goudie, 2001; Prospero et al., 2002; Ginoux et al., 2012). Previous studies (Prospero et al., 2002; Ginoux et al., 2012), have shown that the major portion of the global dust burden originates from the Sahara Desert, which hosts the most intense dust source of the planet, the Bodélé Depression located in the northern Lake Chad Basin. In North Africa, large amounts of mineral particles are also emitted in the Western Sahara while other noticeable sources of smaller spatial extension are located in the eastern Libyan Desert, in the Nubian Desert (Egypt) and Sudan (Engelstaedter et al., 2006).

One of the major dust sources of the planet, following N. Africa, is the Middle East with several active regions (Pease et al., 1998; Hamidi et al., 2013; Yu et al., 2013) in which wind-blown dust is emitted from alluvial plains (Tigris-Euphrates River) and sandy deserts (Rub al Khali Desert). Important dust sources are also recorded in the Asian continent, particularly in the Taklamakan Desert (Ge et al., 2014), in the Gobi Desert (Chen et al., 2017), in its central parts (Karakum Desert; Li and Sokolik, 2018), in the Sistan Basin (Alizadeh Choobari et al., 2013) and in the Thar Desert (Hussain et al., 2005). In North America, mineral particles emitted from the Mojave and Sonoran deserts (Hand et al., 2017) have mainly natural origin while in the Chihuahuan Desert as well as in the Southern Great Plains the anthropogenic interference on soil can favor emission of dust particles and subsequently their entrainment in the atmosphere (Hand et al., 2016). Overall, the major portion of the global dust budget arises from the deserts of the N. Hemisphere (Ginoux et al., 2012) while mineral aerosols are also emitted in Australia (Ekström et al., 2004), South Africa (Bryant et al., 2007; Vickery et al., 2013) and South America (Gassó and Torres, 2019), but to a lesser extent. At global scale, most of the entrained dust loads in the atmosphere originate from tropical and sub-tropical arid regions; however, about 5% of the global dust budget consists of particles emitted from high-latitude sources (Bullard et al., 2016).

Dust plays a key role in several aspects of the Earth system such as climate (e.g. Lambert et al., 2013; Nabat et al., 2015) and weather (Pérez et al., 2006; Gkikas et al., 2018; Gkikas et al., 2019), attributed to the perturbation of the Earth-Atmosphere system radiation budget (Sokolik and Toon, 1996; Haywood and Bucher, 2000) by mineral particles, the productivity of oceanic waters (Jickells et al., 2005) and terrestrial ecosystems (Okin et al., 2004), and effects on humans' health (Kanatani et al., 2010; Kanakidou et al., 2011; Pérez García-Pando et al., 2014; Du et al., 2016, Querol et al., 2019). Dust is characterized by a pronounced temporal and spatial variability due to the heterogeneity of the emission, transport and deposition processes governing its life cycle (Schepanski, 2018). A variety of atmospheric circulation mechanisms, spanning from local to planetary scales, are responsible for the uplifting of erodible particles from bare soils (Koch and Renno, 2005; Knippertz et al., 2007; Klose and Shao, 2012; Fiedler et al., 2013) and their subsequent transport (Husar et al., 2001; Prospero and Mayol-Bracero, 2013; Yu et al., 2015; Flaounas et al., 2015; Gkikas et al., 2015), accumulation and removal (Zender et al., 2003; Ginoux et al., 2004) from the atmosphere.

Given the scientific importance of dust in the Earth system as well as the numerous socioeconomic impacts (Stefanski and Sivakumar, 2009; Weinzierl et al., 2012; Kosmopoulos et al., 2018), there is a need to monitor and forecast dust loads at different spatiotemporal scales. Contemporary satellite observations, available over long-term periods, have been proven a powerful tool in such efforts as they provide wide spatial coverage, relatively high sampling frequency and considerably high accuracy. Spaceborne retrievals have been widely applied in aerosol research for the description of dust load features and their evolution (e.g., Kaufman et al., 2005; Liu et al., 2008; Peyridieu et al., 2013; Rashki et al., 2015; Gkikas et al., 2013; 2016; Marinou et al., 2017; Proestakis et al., 2018). Even more accurate aerosol observations, but locally restricted, are derived by ground-based platforms consisting of sunphotometers, lidars and in-situ instruments. Based on these measurements, columnar optical and microphysical properties of mineral particles have been analyzed extensively (Giles et al., 2012), altitude-resolved information of optical properties has provided insight about the dust vertical distribution (Mamouri and Ansmann, 2014), and a comprehensive description of dust optical, microphysical and chemical properties has been achieved from surface and aircraft in-situ instruments (Rodríguez et al., 2012; Liu et al., 2018). Finally, through the deployment of atmospheric-dust models (e.g., Pérez et al., 2011; Haustein et al., 2012), global (e.g., Ginoux et al., 2004) and regional (e.g., Basart et al., 2012) displays of dust burden are provided.

Traditionally, observations have been utilized to evaluate and eventually constrain model performance. Observations are increasingly used in data assimilation (DA) schemes for aerosol forecast initialization (Di Tomaso et al., 2017) and development of reanalysis datasets (Benedetti et al., 2009; Lynch et al., 2016; Gelaro et al., 2017). The most exploited reanalysis datasets in dust-

related studies, are the MERRAero (Modern Era Retrospective analysis for Research and Applications Aerosol Reanalysis; Buchard et al., 2015) and its evolution MERRA-2 (Modern-Era Retrospective analysis for Research and Applications, Version 2; Gelaro et al., 2017) as well as CAMSRA (Copernicus Atmosphere Monitoring Service Reanalysis; Inness et al., 2019) and its predecessor MACC (Monitoring Atmospheric Composition and Climate; Inness et al., 2013). Current reanalysis datasets provide information about dust aerosols at high temporal resolution and decadal time scales. However, even though AOD observations are assimilated, the performance of the simulated outputs is partly model-driven and their resolution is relatively coarse.

The overarching goal of the present study is to describe the development of the MIDAS (ModIs Dust AeroSol) dataset providing dust optical depth (DOD) over a 15-year period (2003-2017). The powerful element of this product is its availability at fine spatial resolution (0.1° x 0.1°) and on a daily basis as well as the provision of full global coverage (i.e., both over land and ocean). Ginoux et al. (2012) analyzed DOD at the same spatial resolution and for a long-term period but restricted the analysis to continental surfaces as the scientific focus was put on the identification of natural and anthropogenic dust sources. Voss and Evan (2020) combined satellite (MODIS, AVHRR) aerosol retrievals and MERRA-2 winds to analyze DOD at coarse spatial resolution (1° x 1°) for extended time periods. CALIOP-based vertical dust backscatter and extinction profiles along with the respective column integrated DODs at 1° x 1° spatial resolution are distributed via the LIVAS database (Amiridis et al., 2015). Taking advantage of the spectral signature of dust at thermal infrared (TIR) wavelengths, DOD is also provided by IASI (Vandenbussche et al., 2013; Capelle et al., 2018; Clarisse et al., 2019) and SEVIRI (Ackerman, 1997) instruments aboard the polar-orbit METOP satellites and the geostationary MSG satellite, respectively. In this case, the conversion of DOD from TIR to mid-visible spectrum range is subjected to several assumptions related to size and other properties. Dust observations from IASI are provided at global scale twice per day and those of SEVIRI cover the hemisphere centered at the prime meridian over the equator every 15 minutes (Schepanski et al., 2012). Thanks to their high sampling frequency, fine spatial resolution and long-term availability, the aforementioned datasets have been used for the identification of dust sources activation across N. Africa (Schepanski et al., 2007; Vandenbussche et al., 2020). Based on the current status described above, MIDAS dataset expands, complements and upgrades existing observational capabilities of dust aerosols being suitable for research studies related to climatology, model evaluation and data assimilation.

For the development of the fine resolution MIDAS DOD, a synergy of MODIS-Aqua (Section 2.1), MERRA-2 (Section 2.2), LIVAS (Section 2.3) and AERONET (Section 2.4) aerosol products has been deployed by exploiting the strong capabilities of each dataset. Based on the applied

136   methodology (Section 3.1), the DOD is calculated by the product of MODIS-Aqua Level 2 AOD and

137   the collocated DOD-to-AOD ratio from MERRA-2. The uncertainty of the DOD is calculated by

138   combining the uncertainties of MODIS AOD and MERRA-2 dust fraction (MDF), using AERONET

139   and LIVAS, respectively, as reference (Section 3.2). We thoroughly compare MDF against the

140   LIVAS dust portion in Section 4.1. The MIDAS DOD is evaluated against AERONET in Section 4.2

141   and compared with MERRA-2 and LIVAS DODs in Section 4.3. In section 4.4, we provide the annual

142   and seasonal global geographical distributions of the MIDAS DOD as a demonstration of the

143   developed product. Finally, the main findings are summarized and the conclusions are drawn in

144   Section 5.

145

146   **2. Datasets**

147   *2.1. MODIS*

148

149   The MODerate resolution Imaging Spectroradiometer (MODIS) is a passive sensor measuring

150   the top of atmosphere (TOA) reflectance in order to retrieve aerosol optical depth (AOD), among

151   other aerosol optical properties, at various wavelengths spanning from the visible to the near infrared

152   spectrum range. MODIS, mounted on the NASA's twin polar satellites Terra and Aqua, acquires

153   high-quality aerosol data since 2000 and 2002, respectively, while thanks to its wide swath (~2330

154   km) provides near-global observations almost on a daily basis. The derivation of AOD is achieved

155   through the implementation of two retrieval algorithms based on the Dark Target (DT) approach,

156   valid over oceans (Remer et al., 2002; 2005; 2008) and vegetated continental areas (Levy et al., 2007a;

157   2007b; 2010) but relying on different assumptions and bands, and the Deep Blue (DB) approach (Hsu

158   et al., 2004; Sayer et al., 2013) providing retrievals over all cloud-free and snow-free land surfaces,

159   including arid and semi-arid surfaces. MODIS datasets are organized into various collections

160   depending on the version of the retrieval algorithms, and into a number of levels depending on their

161   spatial and temporal resolution. For our purposes, we are utilizing Collection 6.1 (C061) MODIS-

162   Aqua Level 2 (L2) retrievals over the period 2003-2017, which are reported at 5-min swath granules

163   (Levy et al., 2013) and are accessible from the Level-1 and Atmosphere Archive & Distribution

164   System (LAADS) Distributed Active Archive Center (DAAC)

165   (https://ladsweb.modaps.eosdis.nasa.gov/). All the updates applied in the latest version of MODIS

166   DB and DT retrievals with respect to Collection 6 are provided in the relevant technical documents

167   available at the Atmosphere Discipline Team Imager Products webpage (https://atmosphere-

168   imager.gsfc.nasa.gov/documentation/collection-61).

169   Each MODIS swath is composed of 203 x 135 retrievals with increasing pixel size from the nadir
170   view (10 km x 10 km) towards the edge of the satellite scan (48 km x 20 km), and to which a Quality
171   Assurance (QA) flag is assigned (Hubanks, 2018). More specifically, these bit values represent the
172   reliability of the algorithm output and are equal to 0 ("No Confidence"), 1 ("Marginal"), 2 ("Good")
173   and 3 ("Very Good"). MODIS AOD retrievals are acquired based on different algorithms according
174   to the underlying surface type. In order to fill observational gaps, attributed to the assumptions or
175   limitations of the applied MODIS algorithms, the DT-Ocean (QA≥1), DT-Land (QA=3) and DB-
176   Land (QA≥2) AOD retrievals are merged based on the Normalized Difference Vegetation Index
177   (NDVI) and the highest accuracy criterion (Sayer et al., 2014). This "merged" AOD is stored in the
178   scientific data set (SDS) named "AOD_550_Dark_Target_Deep_Blue_Combined", which is
179   extracted and processed for the needs of the current work. Finally, two quality filtering criteria are
180   applied to the raw MODIS AODs for eliminating observations which may be unreliable. AODs
181   associated with cloud fraction (CF) higher than 0.8 as well as those with no adjacent retrievals are
182   masked out following the recommendations of previous studies (Anderson et al., 2005; Zhang and
183   Reid, 2006; Hyer et al., 2011; Shi et al., 2011). The first criterion is associated with the potential
184   cloud contamination on AODs while the second one discards "suspicious" retrievals from the dataset.
185
186   *2.2. MERRA-2*
187
188   The Modern-Era Retrospective Analysis for Research and Applications, version 2 (MERRA-2),
189   developed by the NASA Global Modeling and Assimilation Office (GMAO), is the first atmospheric
190   reanalysis spanning over the new modern satellite era (1980 onward) in which aerosol-radiation
191   interactions and the two-way feedbacks with atmospheric processes are taken into account (Gelaro et
192   al., 2017). The key components of MERRA-2 (Buchard et al., 2017) are the Goddard Earth Observing
193   System (GEOS-5) (Rienecker et al. 2008; Molod et al. 2015), which is radiatively coupled to the
194   Goddard Chemistry Aerosol Radiation and Transport model (GOCART; Chin et al. 2002; Colarco et
195   al. 2010), and the three-dimensional variational (3DVar) Gridpoint Statistical Interpolation analysis
196   system (GSI) (Wu et al. 2002).
197   The GOCART aerosol module simulates emission, sinks, removal mechanisms (dry deposition
198   and gravitational settling, large-scale wet removal and convective scavenging) as well as the chemical
199   processes of five aerosol species: dust, sea-salt, sulfate, and black and organic carbon. Their optical
200   properties are based on the updated Optical Properties of Aerosols and Clouds (OPAC) database
201   (Hess et al. 1998), incorporating dust non-spherical shape (Meng et al. 2010; Colarco et al. 2014),
202   and are calculated according to Colarco et al. (2010). For coarse particles (i.e., dust and sea-salt), five
203   non-interacting size bins are considered whose emissions are driven by the wind speed based on the

parameterizations of Marticorena and Bergametti (1995), for dust, and on the modified version of Gong (2003), for sea-salt. Both hydrophobic and hydrophilic black (BC) and organic (OC) carbon emitted from anthropogenic activities (i.e., fossil fuel combustion) and natural processes (i.e., biomass burning) are considered. Regarding sulfate aerosols (SO_4), these either are primarily emitted or are formed by the chemical oxidation of sulfur dioxide gas (SO_2) and dimethyl sulfide (DMS). Until 2010, daily emissions of eruptive and degassing volcanoes are derived from the AeroCom Phase II project (Diehl et al. 2012; http://aerocom.met.no/) and afterwards only a repeating annual cycle of degassing volcanoes is included in MERRA-2. The hygroscopic growth of sea-salt, sulfate and hydrophilic carbonaceous aerosols is determined by the simulated relative humidity (RH) and the subsequent modification of particles' shape and composition is taken into account in computations of particles' fall velocity and optical parameters (Randles et al., 2017). A detailed description of the emission inventories along with the global climatological maps, representative for the period 2000 – 2014, are given in Randles et al. (2017).

MERRA-2 is a multidecadal reanalysis in which a variety of meteorological and aerosol observations are jointly assimilated (Gelaro et al., 2017). The former group of observations consists of ground-based and spaceborne atmospheric measurements/retrievals summarized in Table 1 of Gelaro et al. (2017) while the full description is presented in McCarty et al. (2016). For aerosol data assimilation, the core of the utilized satellite data is coming from the MODIS instrument multichannel radiances, in addition to observational geometry parameters, cloud fraction and ancillary wind data. Over oceans, AVHRR radiances, from January 1980 to August 2002, are used as well and over bright surfaces (albedo > 0.15) the non-bias-corrected AOD retrieved for the Multiangle Imaging SpectroRadiometer (MISR; Kahn et al., 2005) is assimilated from February 2000 to June 2014. Apart from spaceborne radiances and retrievals, the Level 2 (L2) quality-assured AERONET measurements (1999 – October 2014; Holben et al., 1998) are integrated in the MERRA-2 assimilation system (Goddard Aerosol Assimilation System, GAAS) which is presented in Randles et al. (2017; Section 3). The cloud-free MODIS radiances (DT algorithm, Collection 5) and AVHRR radiances (above oceanic regions) are used for the derivation of bias-corrected AODs, via a neural net retrieval (NNR), adjusted to the log-transformed AERONET AODs. It must be clarified, that only the MERRA-2 AOD is directly constrained by the observations while the model's performance (background forecast) and data assimilation structure (parameterization of error covariances) are "responsible" for the aerosol speciation, among other aerosol diagnostics (Buchard et al., 2017).

In the present study, we use the columnar MERRA-2 total and dust AOD at 550 nm in order to calculate the contribution, in optical terms, of mineral particles to the overall load. The computed dust-to-total AOD ratio (i.e., MDF) is evaluated against LIVAS and then used for the derivation of MIDAS DOD. MERRA-2 products (M2T1NXAER files; V5.12.4; aerosol diagnostics) have been

239 downloaded from the GES DISC server (https://disc.gsfc.nasa.gov/)) and are provided as hourly
240 averages at 0.5° x 0.625° lat-lon spatial resolution.

241

242 2.3. *LIVAS*

243

244 The ESA LIVAS database (Amiridis et al., 2015; http://lidar.space.noa.gr:8080/livas/) contains a
245 pure dust satellite-based product spanning from 2007 to 2015, which has been derived from the Cloud
246 Aerosol Lidar with Orthogonal Polarization (CALIOP) sensor, onboard the Cloud-Aerosol Lidar and
247 Infrared Pathfinder Satellite Observation (CALIPSO) satellite. This active sensor acquires altitude
248 resolved observations of aerosols and clouds since mid-June 2006 (Winker et al., 2010). CALIPSO,
249 flying in the A-Train constellation (Stephens et al., 2002), provides almost simultaneous observations
250 with Aqua thus making feasible and powerful their synergistic implementation for aerosol research.
251 CALIOP, an elastic backscatter two-wavelength polarization-sensitive Nd:YAG lidar in a near-nadir-
252 viewing geometry (since 28th November 2007, 3 degrees off-nadir), emits linearly polarized light at
253 532 and 1064 nm and detects the co-polar components at 532 and 1064 nm and the cross-polar
254 component at 532 nm, relative to the laser polarization plane (Hunt et al., 2009). Based on the
255 attenuated backscatter profiles (Level 1B) and the implementation of retrieval algorithms (Winker et
256 al., 2009), aerosol/cloud profiles as well as layer products are provided at various processing levels
257 (Tackett et al., 2018). CALIOP Level 2 (L2) aerosol and cloud products are provided at a uniform
258 spatial resolution along horizontal (5 km) and vertical (60 m) dimensions. Detectable atmospheric
259 features are first categorized to aerosols or clouds and then are further discriminated into specific
260 subtypes according to Vaughan et al. (2009). For aerosols, in the Version 3 used here, 6 subtypes are
261 considered consisting of clean marine, dust, polluted continental, clean continental, polluted dust and
262 smoke (Omar et al., 2009). Based on the aerosol subtype classification, specific extinction-to-
263 backscatter ratios (Lidar Ratio - LR) are applied for the provision of extinction coefficient profiles
264 along the CALIPSO orbit-track (Young and Vaughan, 2009).

265 In this study we use the CALIOP pure dust product available in the aforementioned LIVAS
266 database (hereafter called the LIVAS dataset), which has been developed according to the
267 methodology described in Amiridis et al. (2013) and updated in Marinou et al. (2017). The
268 aforementioned technique relies on the incorporation of aerosol backscatter coefficient profiles and
269 depolarization ratio, providing a strong evidence of dust presence due to mineral particles' irregular
270 shape (Freudenthaler et al., 2009; Burton et al., 2015; Mamouri and Ansmann, 2017), thus allowing
271 the separation of the dust component from aerosol mixtures. The LIVAS dataset is obtained by
272 applying appropriate regionally-dependent LR values (see Figure S1; Marinou et al., 2017; Proestakis
273 et al. 2018 and references within), instead of the raw universal CALIOP dust LR (40 sr; Version 3),

274 which are multiplied with the dust backscatter coefficient profiles at 532 nm in order to calculate the
275 corresponding extinction coefficient profiles. After a series of strict quality screening filters (Marinou
276 et al., 2017), the columnar total/dust/non-dust optical depths as well as the DOD-to-AOD ratio over
277 the period 2007 – 2015 are aggregated at 1° x 1° grid cells covering the whole globe. The performance
278 of the LIVAS pure DOD product has been assessed against AERONET over N. Africa and Europe
279 (Amiridis et al., 2013) revealing a substantial improvement when the abovementioned
280 methodological steps are applied. The LIVAS pure DOD product has been utilized in variety of
281 research studies, such as the assessment of dust outbreaks (Kosmopoulos et al., 2017; Solomos et al.,
282 2018) and phytoplankton growth (Li et al., 2018), the 4D description of mineral loads over long-term
283 periods (Marinou et al., 2017; Proestakis et al., 2018), the evaluation of dust models (Tsikerdekis et
284 al., 2017; Georgoulias et al., 2018; Konsta et al., 2018) as well as the evaluation of new satellite
285 products (Georgoulias et al., 2016).

286

287 *2.4. AERONET*

288

289   Ground-based observations acquired from the AEronet RObotic NETwork (AERONET; Holben
290 et al., 1998) have been used as reference in this work in order to evaluate the accuracy of the MIDAS
291 DOD product. The evaluation analysis has been performed by utilizing the almucantar (inversion)
292 retrievals, providing information for the total aerosol amount (AOD) as well as for other
293 microphysical (e.g., volume size distribution) and optical (e.g., single scattering albedo) properties
294 (Dubovik and King, 2000; Dubovik et al., 2006). In the present study, focus is put on the aerosol
295 optical properties retrieved at four wavelengths (440, 675, 870 and 1020 nm) utilizing as inputs
296 spectral AODs and sky (diffuse) radiances. More specifically, we used Version 3 (V3) AERONET
297 data (Giles et al., 2019; Sinyuk et al., 2020) of AOD (for total and coarse aerosols), Ångström
298 exponent (α) and single scattering albedo (SSA). For the amount (AOD) and size (α) related optical
299 parameters, only quality assured retrievals (i.e., Level 2; L2) are used, whereas for the SSA, the L2
300 and Level 1.5 (L1.5) observations are merged in order to ensure maximum availability. Unfavourable
301 atmospheric conditions or restrictions on solar geometry result in a reduced amount of inversion
302 outputs compared to the availability of sun-direct measurements or the Spectral Deconvolution
303 Algorithm (SDA; O'Neill et al., 2003) retrievals. Even though the aforementioned AERONET data
304 provide information about aerosol size (i.e. Ångström exponent) or coarse AOD (from SDA
305 retrievals), the optimum approach for identifying dust particles and discriminating them from other
306 coarse particles (i.e., sea-salt) requires the use of SSA as it will be discussed in the next paragraph.

Through the combination of the selected optical properties from almucantar retrievals we achieved the spectral matching between ground-based and spaceborne observations as well as the determination of DOD on AERONET retrievals. Regarding the first part, the $\alpha_{440\text{-}870nm}$ and AOD_{870nm} values are applied in the Ångström formula in order to interpolate the AERONET AOD at a common wavelength (i.e., 550 nm) with MODIS. For the evaluation of DOD, a special treatment of AERONET retrievals is required in order to identify conditions where dust particles either only exist or clearly dominate over other aerosol species. The vast majority of previous studies (e.g., Fotiadi et al., 2006; Toledano et al., 2007; Basart et al., 2009) have relied on the combination of AOD and α for aerosol characterization, associating the presence of mineral particles with low α levels and considerable AODs. Here, we are keeping records where the $\alpha_{440\text{-}870nm} \leq 0.75$ and $SSA_{675nm} - SSA_{440nm} > 0$, without taking into account the aerosol optical depth. The first criterion ensures the predominance of coarse aerosols, while the second one serves as an additional filter for discriminating dust from sea-salt particles, taking advantage of the specific spectral signature of SSA (i.e. decreasing absorptivity for increasing wavelengths in the visible spectrum) in pure or rich dust environments (Giles et al., 2012).

Then, from the coarse AODs at 440, 675 and 870 nm we calculate the corresponding α, which is applied in order to obtain the AERONET coarse AOD at 550 nm. This constitutes the AERONET-derived DOD assuming that the contribution of fine dust particles (particles with radii less than the inflection point in the volume size distribution) is small. Likewise, through this consideration any potential "contamination" from small-size particles of anthropogenic or natural origin (e.g., biomass burning), which is likely far away from the sources, is tempered or avoided.

3. Methods

3.1. Derivation of dust optical depth on MODIS swaths

The core concept of our approach is to derive DOD on MODIS L2 retrievals, provided at fine spatial resolution, via the synergy with the MERRA-2 products. More specifically, the MERRA-2 dust fraction (MDF) to total AOD_{550nm} (Eq. 1) is multiplied with the MODIS AOD_{550nm} in order to calculate DOD_{550nm} at swath-level (Eq. 2).

$$MDF = \frac{AOD_{DUST;MERRA-2}}{AOD_{TOTAL;MERRA-2}} \textbf{ (Eq. 1)}$$

$$DOD_{MODIS} = AOD_{MODIS} * MDF \textbf{ (Eq. 2)}$$

To achieve that, the datasets are collocated temporally and spatially. MERRA-2 outputs are provided at coarse spatial resolution (0.5° x 0.625°) in contrast to MODIS-Aqua observations (10 km

342 x 10 km). MODIS swaths are composed by 203 x 135 retrievals and for each one of them we compute

343 the nearest distance from the MERRA-2 grid points, considering the closest hourly time step to

344 MODIS overpass time. Then, the MDF is used to calculate the DOD from the AOD on MODIS swath

345 native grid. Our approach avoids on purpose the inclusion of additional optical properties providing

346 information on aerosol size (α) available from MODIS and absorptivity (Aerosol Index; Torres et al.,

347 1998) from OMI that are characterized by inherent limitations. Previous evaluation studies (Levy et

348 al., 2013; Sayer et al., 2013) have shown that size parameters acquired by MODIS are highly

349 uncertain, particularly over land and at low AOD conditions. In addition, since early 2008, the OMI

350 sensor has lost half of its swath due to the "row-anomaly" issue (Torres et al., 2018) thus "hampering"

351 the MODIS-OMI collocation when it is attempted at fine spatial resolution.

352

353 *3.2 Uncertainty estimation*

354

355 As expressed in Eq. 2, the MIDAS DOD results from the product of MODIS AOD and MDF. The

356 uncertainty of the DOD product (Δ(DOD)) accounts for the corresponding uncertainties of the AOD

357 and MDF, which are calculated using AERONET and LIVAS, respectively, as a reference. The

358 mathematical expression of the Δ(DOD), given in Eq. 3, as follows, results from the implementation

359 of the product rule on Eq. 2.

360

361 $$\Delta(DOD) = \Delta(AOD) * MDF + AOD * \Delta(MDF) \ (\textbf{Eq. 3})$$

362 The term Δ(AOD) defines the expected error (EE) confidence envelope in which ~68% of the

363 MODIS-AERONET AOD differences are expected to fall within. This term varies depending on the

364 applied MODIS aerosol retrieval algorithm.

365 For each of the two DT retrieval algorithms, we use the corresponding linear equations expressing

366 Δ(AOD) with respect to AERONET AOD over ocean (Levy et al., 2013; Eq. 4) and land (Levy et al.,

367 2010; Eq. 5). For the DB AOD land retrievals (Eq. 6), we use the formula for prognostic uncertainty

368 estimates given in Sayer et al. (2013) but with updated coefficients a and b for C061 data varying

369 between   vegetated   and   arid   surface   types   (https://atmosphere-

370 imager.gsfc.nasa.gov/sites/default/files/ModAtmo/modis_deep_blue_c61_changes2.pdf).   More

371 specifically, over vegetated land, a and b are equal to 0.079 and 0.67, respectively, while the

372 corresponding values over barren soils are equal to 0.12 and 0.61. The land cover classes have been

373 extracted from the International Geosphere-Biosphere Programme (IGBP) database available via the

374 MCD12C1 data (https://lpdaac.usgs.gov/products/mcd12c1v006/). For the merged (DB+DT) land

375 AOD, the uncertainty is estimated via the square root of the quadrature sum of the DT-Land and DB-

376 Land uncertainties divided by two (Eq. 7).

377

$$\Delta(AOD_{DT-Ocean}) = \pm(0.10 * AOD + 0.04) \text{ (Eq. 4)}$$

$$\Delta(AOD_{DT-Land}) = \pm(0.15 * AOD + 0.05) \text{ (Eq. 5)}$$

$$\Delta(AOD_{DB-Land}) = \pm\left(\frac{a+b*AOD}{AMF}\right) \text{ (Eq. 6)}$$

$$\Delta(AOD_{DTDB-Land}) = \pm\frac{\sqrt{[\Delta(AOD_{DT-Land})]^2+[\Delta(AOD_{DB-Land})]^2}}{2} \text{ (Eq. 7)}$$

Before proceeding with the calculation of the $\Delta(DOD)$, few key aspects must be highlighted for the sake of clarity. In equations 4 and 5, the AOD uncertainty is defined as a diagnostic error since it is calculated utilizing AERONET as reference. Here, we are using the same equations replacing AERONET AODs with those given by MODIS. This relies on the fact (results not shown here) that their averages from a global perspective are almost unbiased; however, at regional level, small negative or positive offsets (lower than 0.05 in absolute terms) are recorded in the vast majority of AERONET sites, thus supporting our argument. For the ocean AOD uncertainty, the defined EE margins (Levy et al., 2013) have been modified in order to sustain symmetry by keeping the upper bound (i.e., thus including more than 68% of expected MODIS-AERONET pairs within the EE). Sayer et al. (2013) estimated the uncertainty of DB AOD by taking into account the geometric air mass factor (AMF) resulting from the sum of the reciprocal cosines of the solar and viewing zenith angles (Eq. 6).

The LIVAS dust fraction is our reference for estimating the MDF uncertainty. The analysis is performed at 1° x 1° spatial resolution considering only grid cells in which both MERRA-2 and LIVAS DODs are higher than or equal to 0.02. According to this criterion, more than 450000 LIVAS-MERRA-2 collocated pairs have been found that are sorted (ascending order) based on MDF (ranging from 0 to 1) and then are grouped in equal size bins containing 20000 data for each sub-sample. For every group, we computed the median MDF (x axis) as well as the 68th percentile of the absolute MERRA-2 – LIVAS dust fraction (y axis) and then we found the best polynomial fit (Eq. 8).

$$\Delta(MDF) = \pm(2.282 * MDF^4 - 6.222 * MDF^3 + 4.700 * MDF^2 - 0.969 * MDF + 0.199) \text{ (Eq. 8)}$$

Depending on the selected MODIS algorithm, the appropriate combination between AOD (Eqs. 4, 5, 6 and 7) and MDF (Eq. 8) uncertainties is applied to calculate the $\Delta(DOD)$ (Eq. 3) on each daily measurement (i.e., DOD) at each grid cell. These pixel-level DOD uncertainties are averaged over the entire study period as well as for each season and the obtained findings will be discussed along with the global spatial patterns (Section 4.5) of dust optical depth in order to provide a measure of the reliability of the derived MIDAS DOD product.

410

411

4. Results

413

On the following sections, a series of analyses including the evaluation of MDF with respect to LIVAS (Section 4.1), the evaluation of MIDAS DOD versus AERONET observations (Section 4.2) as well as an intercomparison among MIDAS, LIVAS and MERRA-2 DODs (Section 4.3), is presented. All the aforementioned steps are performed in order to justify the validity of the applied methodology and to understand its limitations. In the last section (4.4), the global annual and seasonal DOD patterns are presented as a demonstration of the MIDAS dataset, and the obtained spatiotemporal features are briefly discussed. The detailed climatological study is provided in a companion paper.

422

4.1. Evaluation of MERRA-2 dust fraction versus LIVAS

424

The evaluation of the MDF is a critical step of our analysis since it is used as the scaling factor of the MODIS AOD for the derivation of the MIDAS DOD. For this reason, the corresponding columnar parameter provided by LIVAS (see Section 2.3) is used as reference. It must be highlighted that the only existing evaluation studies of MERRA-2 aerosol products have been performed either for specific aerosol species or limited time periods (e.g., Buchard et al., 2017; Veselovskii et al., 2018) or for the total load (e.g., Mukkavilli et al., 2019; Sun et al., 2019) in specific regions showing the ability of MERRA-2 in reproducing the integrated aerosol fields. Nevertheless, the speciation of the suspended particles, which is to a large extent determined by the model physics assumptions (Gelaro et al., 2017), has not been thoroughly evaluated. Therefore, the present analysis complements and expands further the existing works providing insight about the performance of MERRA-2 in terms of discriminating among aerosol types (particularly for dust) and subsequently estimating their contribution to the total atmospheric load.

Figure 1 depicts the geographical distributions of the dust-to-total AOD ratio, based on MERRA-2 (i) and LIVAS (ii) averaged over the timeframe (2007-2015) of the LIVAS dataset. The corresponding maps of mean bias, fractional bias (FB), fractional gross error (FGE) and correlation coefficient (R) are given in Figure 2. For consistency, we regridded the MERRA-2 data to 1° x 1° spatial resolution and selected the closest output to the CALIOP overpass time only during daytime hours when aerosol retrievals obtained by passive sensors at visible wavelengths are assimilated. At a first glance, the spatial patterns are very similar, particularly in areas where the presence of dust is predominant. Across the "dust belt" (Prospero et al., 2002), the most evident deviations (MDF

445   underestimation by ~0.1 or 10%) are recorded in the borders of Afghanistan and Pakistan (Dasht-e

446   Margo and Kharan Deserts) as well as in the Taklamakan Desert (Fig. 2-i). However, the FB (Fig. 2-

447   ii) and FGE (Fig. 2-iii) metrics (Yu et al., 2006), which are less affected by outliers compared to the

448   bias, are close to zero (ideal score) in most of the aforementioned regions, thus indicating a very good

449   performance of MERRA-2. In terms of temporal covariation (Fig. 2-iv), moderate R values (0.5-0.6)

450   are obtained in land areas where the presence of dust is predominant, with the exception of the western

451   parts of Sahara where the correlation levels are slightly higher than zero. Due to the complex and

452   highly variable nature of the emission processes and therefore the poorer behavior of the model, the

453   correlation tends to be smaller over the main dust sources throughout the year (right column in Figure

454   S2). In downwind regions of the N. Hemisphere, particularly over the main transport pathways (i.e.,

455   Atlantic Ocean, Mediterranean, Arabian Sea, E. Asia), correlation substantially increases (up to 0.9).

456   In addition, FB and FGE metrics reveal a good performance by MERRA-2; which, however,

457   downgrade for increasing distances from the sources due to the weaker dust contribution to the total

458   aerosol load. An exception is observed for the mean bias along the tropical Atlantic Ocean where the

459   MDF is overestimated by up to 10% in the eastern parts in contrast to longitudes westward of 45° W

460   where zero biases or slight underestimations (~5%, Caribbean Sea) are obtained.

461   A discrepancy between the LIVAS and MERRA-2 dust portion is found in the Mojave, Sonoran,

462   Chihuahuan desert areas extending between southwestern US and northern Mexico. As shown in

463   Figure 1, the dust contribution given by LIVAS in those areas is more widespread and stronger in

464   contrast to MERRA-2, which simulates less dust amount over the sources (Mojave Desert) and the

465   surrounding regions (maximized during DJF and MAM; Fig. S2). According to the evaluation metrics

466   in those areas (Figure 2), the MDF underestimation ranges between 20% to 50%, negative FB (down

467   to -1) and high FGE values (locally exceeding 1) are evident while the correlation levels are low,

468   particularly over Mexico. In the S. Hemisphere, the deficiency of MERRA-2 is pronounced along the

469   western coasts of S. America as well as in the Patagonian and Monte Deserts, particularly during JJA

470   and SON (Fig. S2), both situated in Argentina. Similar results are found in S. Africa while in Australia

471   a contrast between its western/eastern and central parts with slight MDF underestimations and

472   overestimations, up to 20% in absolute terms, respectively, are recorded (Figure 2-i). Nevertheless,

473   the agreement between MERRA-2 and LIVAS in temporal terms is supported by the moderate-to-

474   high R values over the "hotspot" regions (Figure 2-iv). Outside of the main dust-affected regions, an

475   obvious discrepancy is found in the eastern Canada and northeastern Russia where MDF yields very

476   low values (< 20%) in contrast to LIVAS reaching values of dust fraction up to 50%. Due to their

477   geographical position, the occurrence of dust loads might not be frequent there, however, their

478   contribution to the total load can be significant under low AOD conditions, which are mainly recorded

479   in the region. This might indicate a poor representation by MERRA-2. However, potential cloud

480   contaminations in the lidar signals, affecting LIVAS reliability, must also be taken into account.

481   The obtained discrepancies are mainly driven by the partial representation of dust sources in

482   MERRA-2 resulting in potentially underestimated dust emission and subsequently to lower dust

483   contribution to the total burden. Dust is originated either from natural (arid lands, salt lakes, glacial

484   lakes) or from anthropogenic sources (Ginoux et al., 2012). Nevertheless, dust sources in MERRA-2

485   are based on Ginoux et al. (2001) accounting mostly for natural dust emission areas. This could partly

486   explain the higher LIVAS dust contribution levels that are also evident on the seasonal distributions

487   where the inter-annual variability of dust fraction is illustrated (Figure S2). Interestingly, most of the

488   MDF underestimations (i.e. bluish colors in Figure 2-i) are recorded in mountainous areas. Depending

489   on the homogeneity of the atmospheric scene over regions characterized by complex topography,

490   variations in the optical paths of subsequent CALIPSO L2 profiles considered in the LIVAS product

491   may result in unrealistic DOD and AOD values. Previous evaluation studies (e.g., Omar et al., 2013)

492   have shown that CALIOP underestimates AOD with respect to ground-based AERONET retrievals,

493   particularly over desert areas (Amiridis et al., 2015), which was attributed primarily to the incorrect

494   assumption of the lidar ratio (LR) (Wandinger et al., 2010) and secondarily to the inability of the lidar

495   to detect thin aerosol layers (particularly during daytime conditions due to the low signal-to-noise

496   ratio). The former factor is related to aerosol type and for Saharan dust particles the necessary increase

497   of LR (from 40 to 58 sr) improved substantially the level of agreement with AERONET and MODIS

498   (Amiridis et al., 2013). Similar adjustments (increments) to the raw LR values, which are highly

499   variable (Müller et al., 2007; Baars et al., 2016), considered in the CALIOP retrieval algorithm have

500   been applied in the LIVAS product over other source areas of mineral particles (see Section 2.3;

501   Figure S1). An additional factor that must be taken into account is the number of MERRA-2 – LIVAS

502   pairs that are used for the metrics calculation. The corresponding global geographical distribution

503   (Figure S3-i), calculated over the period 2007-2015, shows that in areas where the model-satellite

504   agreement is good (Figure 2) the number of common samples is high (>100) in contrast to regions

505   with a low number of common samples (<50) where the computed metrics are degraded.

506   In order to complete the evaluation of the MDF versus LIVAS, the dependency of the level of

507   agreement on the spatial representativeness within the 1°x1° LIVAS grid-cell has also been

508   investigated. Figure S3-ii displays the long-term averaged geographical distribution of the number of

509   CALIOP L2 profiles (up to 24) aggregated for the derivation of the LIVAS 1°x1° grid-cell. According

510   to the global map, the maximum number is recorded in the latitudinal band extending from 45° S to

511   45° N while the "impact" of extended clouds around the equator is apparent. Outside this zone, the

512   number of profiles used is mainly less than 14 and decreases towards the poles due to the enhanced

513   cloudiness. The same evaluation metrics presented in Figure 2 have been computed also at planetary

514   scale for individual classes of CALIOP L2 number of profiles (Figure S4) aggregated for the

515   derivation of the LIVAS 1° x 1° grid cells. Overall, about 3.4 million pairs (x tick named "ALL" in

516   Figure S4-a) have been found over the period 2007-2015 and are almost equally distributed for bins

517   spanning from 8 to 20 while the number of collocated data is higher in the lowermost (≤ 7) and

518   uppermost (≥ 21) tails of the distribution. The FB (Figure S4-c), FGE (Figure S4-d) and correlation

519   (Figure S4-e) results reveal that the consistency between MDF and LIVAS gradually improves for

520   higher grid-cell representativeness. At global scale, MERRA-2 overestimates the dust fraction by up

521   to 1.5% with respect to LIVAS (Figure S4-b, "ALL" sample). Among the bin classes, the MDF-

522   LIVAS differences are mostly positive and lower than ~3% and decrease further when at least 12

523   CALIOP profiles are aggregated for the derivation of the LIVAS grid cell.

524

525   *4.2. Evaluation of MIDAS DOD versus AERONET*

526

527   In the present section, we provide an evaluation of the MIDAS DOD against the corresponding

528   AERONET product (Section 2.4). An illustration of the MODIS-AERONET collocation method (an

529   example from aerosol optical depth without applying the criteria for DOD) is shown in Figure S5.

530   The obtained results at global and station level are presented in Figures 3 and 4, respectively. As

531   expected, the number of coincident spaceborne and ground-based DODs collected at 436 AERONET

532   stations (red circles in Figure 3-i) is low (10478 pairs) due to the limited amount of almucantar

533   retrievals and the implementation of filters for the determination of DOD in AERONET data.

534   According to the global scatterplot metrics (Figure 3-ii), a very good performance of the MIDAS

535   DOD is revealed since both datasets are well correlated (R=0.89) with MIDAS only slightly

536   overestimating DOD compared to AERONET (0.004 or 2.7%). Only AERONET AODs associated

537   with α lower/equal than/to 0.75 are kept for the evaluation procedure. While this threshold is higher

538   compared to previous applied cut-off levels (e.g. Dey et al., 2004; Tafuro et al., 2006; Reid et al.,

539   2008; Kim et al., 2011; Gkikas et al., 2016), our global scatterplot metrics are very similar when

540   reducing α from 0.75 to 0.25 (results not shown here).

541   The evaluation analysis was also performed for each station individually. Figure 4 depicts only

542   sites with at least 30 coincident MIDAS-AERONET observations, thus making meaningful the

543   comparison at station level. This criterion is satisfied in 86 stations, which overall comprise 77% (or

544   8095) of the total population of coincident DODs, and are mostly located over dust sources as well

545   as in areas affected by dust transport. Figure 4-i shows the station-by-station variability of the number

546   of common MIDAS/AERONET observations ranging from 100 to 457 (Banizoumbou, Niger) across

547   N. Africa and the Middle East whereas in the remaining sites is mainly lower than 70. Between the

548   two datasets, very high R values (up to 0.98) are found in N. Africa, the Middle East, outflow regions

549 (Cape Verde, Canary Islands, Mediterranean) and at distant areas (Caribbean Sea) affected by long-

550 range transport. Across the Sahel, maximum RMSE levels (up to 0.26) are recorded (Figure 4-iii) due

551 to the intense loads and strong variability of the Saharan dust plumes. Regarding biases, positive

552 deviations of up to 0.08 are computed in most AERONET sites in the area while the largest negative

553 offsets (down to -0.14) are recorded at the stations of Ilorin and Djougou (near to the coasts of the

554 Gulf of Guinea) in agreement with Wei et al. (2019b). Several reasons may explain the obtained

555 MIDAS-AERONET differences over the above-mentioned stations taking into account that the MDF

556 is generally well reproduced. The first one is related to the MODIS retrieval algorithm itself and more

557 specifically to the applied aerosol models, surface reflectance and cloud screening procedures (Sayer

558 et al., 2013). The second factor is the omission of fine DOD in AERONET data, which would likely

559 reduce the positive biases. However, its contribution to the total dust AOD is difficult and probably

560 impossible to be quantified accurately. Similar tendencies are found for RMSE and bias in the Middle

561 East where the satellite and ground-based DODs are in general well-correlated. In the Mediterranean,

562 the temporal covariation between the two datasets is quite consistent (R>0.8) with the MIDAS DOD

563 being slightly underestimated probably due to the MDF underestimation (mainly recorded in JJA;

564 Fig. S2).

565   In Asia, few stations are available with sufficient number of MIDAS-AERONET matchups in

566 which the slight positive and the negative DOD biases (Figure 4-iv) are generally consistent with

567 those of AOD (results not shown here). This indicates that the MODIS AOD offsets are "transferred"

568 to MIDAS DOD, which is also affected by the MDF underestimation (Figure 2-i). In the southwestern

569 United States, the evaluation scores at 12 AERONET sites show a moderate performance of the

570 derived DOD (R: 0.28-0.94, bias: -0.034-0.003, RMSE: 0.02-0.04) attributed to the deficiency of

571 MERRA-2 to reproduce adequately the contribution of dust particles to the total aerosol load in

572 optical terms. Finally, our assessment analysis in the Southern Hemisphere for stations located in

573 Argentina, Namibia and Australia, reveals MIDAS-AERONET deviations, spanning from -0.03

574 (Cordoba-CETT) to 0.02 (Gobabeb), and correlations ranging from 0.14 (Fowlers_Gap) to 0.96

575 (Canberra).

576

577 *4.3. Intercomparison of MIDAS, MERRA-2 and LIVAS DOD products*

578

579   Following the evaluation of MIDAS DOD against AERONET, the MIDAS, MERRA-2 and

580 LIVAS DOD products are investigated in parallel. For this purpose, the MERRA-2 and MIDAS data

581 have been regridded to 1° x 1° grid cells between 2007 and 2015 to match the spatial resolution and

582 availability of LIVAS. Then, the three datasets have been collocated spatially and temporally. The

583 intercomparison has been performed only during daytime conditions and the obtained findings are

584 presented through geographical distributions (Section 4.3.1) and average monthly timeseries of

585 regional, hemispherical and planetary averages (Section 4.3.2). Finally, it must be clarified that our

586 focus in this part of the analysis is the intercomparison among the DOD products and not to interpret

587 their spatiotemporal features. The latter will be discussed thoroughly in a companion paper analyzing

588 the MIDAS fine resolution DOD dataset.

589

590   4.3.1. *Geographical distributions*

591

592   The annual geographical distributions of LIVAS, MERRA-2 and MIDAS DODs are depicted in

593 Figures 5-i, 5-ii and 5-iii, respectively, while the corresponding global seasonal maps are provided in

594 Figure S6. Among the three datasets, both for annual and seasonal geographical distributions, it is

595 apparent a very good agreement in spatial terms in contrast to the magnitude of the simulated

596 (MERRA-2) and retrieved (MIDAS, LIVAS) DODs. The most evident differences of MERRA-2

597 (Figure 5-ii) and MIDAS (Figure 5-iii), with respect to LIVAS (Figure 5-i), are encountered across

598 N. Africa forming clear patterns with positive and negative deviations over the Sahara and the Sahel,

599 respectively. In particular, MERRA-2 DOD positive offsets mostly range from 0.04 to 0.20 while

600 those of MIDAS-LIVAS are lower; placing our DOD product between active remote sensing

601 retrievals and reanalysis dataset. Previous studies relying on satellite (Yu et al., 2010; Kittaka et al.,

602 2011; Ma et al., 2013) and ground-based (Schuster et al., 2012; Omar et al., 2013) observations have

603 reported that CALIOP underestimates AOD over the Sahara. Konsta et al. (2018), who utilized higher

604 and more realistic dust lidar ratio (55 sr; adopted also for the region in the current study) compared

605 to the aforementioned works (40 sr), reported similar tendencies of lower magnitude against MODIS.

606 Therefore, additional factors might contribute to the lower lidar-derived DODs over the arid regions

607 in N. Africa. For example, it has been observed that CALIOP can misclassify as clouds very intense

608 dust layers which on the other hand can attenuate significantly or totally the emitted laser beam (Yu

609 et al., 2010; Konsta et al., 2018). All these aspects, most likely met over dust sources, act towards

610 reducing DOD (resulting from the vertical integration of the extinction coefficient profiles) and might

611 explain the "missing" hotspot by LIVAS in/around the Bodélé Depression in contrast to single-view,

612 multi-angle and geostationary passive satellite sensors (e.g., Banks and Bridley, 2013; Wei et al.,

613 2019a). Across the Sahel, LIVAS provides higher DODs (mainly up to 0.2) against both simulated

614 and satellite products. These differences might be attributed to the misrepresentation of dust sources

615 in MERRA-2 along this zone where vegetation cover has a prominent seasonal cycle (Kergoat et al.,

616 2017). An inaccurate representation of vegetation also impacts the surface reflectance which in turn

617 can introduce critical errors in the MODIS retrieval algorithm. Wei et al. (2019b) showed that MODIS

618 underestimates AOD with respect to AERONET in that region, which is in agreement with the fact

619   that the maximum MIDAS-AERONET negative DOD differences are found at Ilorin and Djougou

620   sites (Figure 4-iv).

621   Over the eastern Tropical Atlantic Ocean, the difference between LIVAS and MIDAS is

622   negligible whereas MERRA-2 gives lower DODs by up to 0.08. In the Middle East, MERRA-2 and

623   MIDAS DODs are higher than in LIVAS over the Tigris-Euphrates basin while an opposite tendency

624   for MERRA-2 is found in the interior parts of Saudi Arabia. Lower DODs are also given by LIVAS

625   over the arid/semi-arid regions eastwards of the Caspian Sea, including also the Aral Sea. This area

626   of the planet is one of the most challenging for spaceborne passive observations due to the terrain

627   complexity prohibiting the accurate characterization of the surface reflectance and type, resulting in

628   unrealistically high MODIS AODs (Klingmüller et al., 2016; see interactive comment posted by

629   Andrew Sayer) that may also affect MERRA-2 via assimilation. The largest negative MIDAS-LIVAS

630   differences (exceeding 0.2) worldwide are recorded in the Taklamakan Desert whereas the

631   corresponding results between MERRA-2 and LIVAS are somewhat lower. This might be attributed

632   to an inappropriate selection (overestimation) of the lidar ratio taking into account that CALIOP

633   mainly underestimates AOD over the region, dust contribution to the total AOD exceeds 70%

634   (Proestakis et al., 2018) throughout the year, and MDF shows robust consistency (Figure 2).

635   Eastwards of the Asian continent, the situation is reversed and the LIVAS DODs are lower by up to

636   0.2 when compared to MERRA-2 and MIDAS indicating a weaker trans-Pacific transport,

637   predominant during boreal spring (second row in Figure S6), being in agreement with the findings of

638   Yu et al. (2010) and Ma et al. (2013). In the S. Hemisphere, negative MERRA-2-LIVAS and MIDAS-

639   LIVAS differences are computed in Patagonia, attributed to the underperformance of MDF, which

640   are not however spatially coherent. On the contrary, in the desert areas of the inland parts of Australia,

641   there is a clear signal of positive MERRA-2-LIVAS deviations, not seen between MIDAS and

642   LIVAS, most likely attributed to the overestimation of aerosol (dust) optical depth by MERRA-2 as

643   it has been recently presented by Mukkavilli et al. (2019). On a global and long-term perspective,

644   based on ~440000 collocated data, MERRA-2 agrees slightly better with LIVAS than MIDAS as it

645   is revealed by the correlation (R=0.74 vs. 0.71) and bias (8.2% vs. 13.3%) metrics.

646

647   *4.3.2   Planetary, hemispherical and regional intra-annual variability*

648   We compared the monthly variability of the planetary (Figure 6-i) and hemispherical (Figures 6-

649   ii, 6-iii) averages of LIVAS (black curve), MERRA-2 (red curve) and MIDAS (blue curve) DODs.

650   We note that for each considered timescale, the averaging has been made following the upper branch

651   shown in Figure 5 of Levy et al. (2009), where each grid cell is first temporally averaged and the

652   resulting field is spatially averaged. In the N. Hemisphere, the annual cycle of DOD is reproduced by

653   the three datasets with maximum levels in June (0.118 for LIVAS/MERRA-2 and ~0.126 for MIDAS)

and minimum ones in Nov-Dec (0.034-0.040). Nevertheless, the most evident deviations in terms of magnitude are recorded during the high-dust seasons with MIDAS giving slightly higher DODs than MERRA-2 and even higher than LIVAS, particularly during boreal spring. On an annual basis (Table 1), the averaged MERRA-2 and MIDAS DODs for the Northern Hemisphere are equal to 0.056 and 0.060, respectively, and higher than the LIVAS climatological value (0.051). In the S. Hemisphere (Figure 6-iii), DODs range at very low levels (up to ~0.011), attributed to the low amounts of mineral particles emitted from spatially restricted desert areas and the limited dust transport over oceanic regions. Despite the low annual levels (0.008; Table 1) there is an intra-annual cycle pattern not entirely commonly reproduced by the three datasets. In particular, MIDAS and MERRA-2 DODs are maximized in February while the highest levels for LIVAS are recorded in September. For all DOD products, the minimum values are found in May, which are slightly lower than those observed during April-July (austral winter). At global scale (Figure 6-i), the seasonal patterns of DODs are mainly driven by those of the N. Hemisphere, particularly for LIVAS and at a lesser degree for MIDAS and MERRA-2. More specifically, there are two peaks (~0.055, March and June) for MIDAS, flat maximum levels (~0.05) between March and June for MERRA-2 while there is a primary (~0.05) and a secondary (~0.04) maximum in June and March, respectively, in LIVAS. Even though there are month-by-month differences, the LIVAS (0.029), MERRA-2 (0.031) and MIDAS (0.033) global annual DODs are relatively close indicating a sufficient level of agreement among the three datasets (Table 1). The obtained value for MIDAS is 10% higher and within the uncertainty estimate of the global DOD average (0.030±0.005) reported by Ridley et al. (2016).

The consistency among the three DOD datasets, in terms of magnitude and temporal covariation, is highly dependent on the region of interest. Figure 7 shows the defined sub-domains considered in this study, Figure S7 depicts the corresponding intra-annual DOD timeseries, while Table 1 lists the computed annual averages as well as their minimum/maximum values between 2007 and 2015. The best agreement among MIDAS, LIVAS and MERRA-2 is found along the Tropical Atlantic Ocean. In the nearby outflow regions (i.e., ETA), considerably high DODs (> 0.1) are found between January-August, being maximum in June, as indicated by the three datasets, with slight underestimations in MERRA-2 (Fig. S7-k). Over the western Tropical Atlantic Ocean, the sharp increase of DOD from May to June indicates the arrival of considerable amounts of Saharan particles, which are sustained at high levels in summer and diminish during autumn and winter (Fig. S7-q). This seasonal fluctuation is almost identically reproduced by the three products. Nevertheless, when the dust activity is well established in the area (i.e., boreal summer), LIVAS shows higher values than MERRA-2 and MIDAS.

Across N. Africa, and particularly in the Bodélé (Fig. S7-a) and W. Sahara (Fig. S7-h), the LIVAS DODs are substantially lower when compared to MIDAS and MERRA-2. In the Bodélé, this is

689   evident for the entire year and in W. Sahara it can be clearly seen between March and June. Similar

690   findings are drawn either for other source areas, such as Central Asia (Fig. S7-c), or outflow regions,

691   such as the Mediterranean (Fig. S7-m). In SUS (Fig. S7-e), the seasonal variation of DODs is in a

692   very good agreement between MERRA-2 and MIDAS but a positive offset is seen for the reanalysis

693   data. On the contrary, LIVAS does not reproduce the secondary maximum in July while it gives very

694   high DODs in Nov-Dec, which are not reliable. Over the Taklamakan (Fig. S7-f), the LIVAS DODs

695   are higher than the corresponding MIDAS and MERRA-2 regional averages in the high-dust months

696   (i.e., April-May) and in July. On the contrary, in the Gobi Desert residing eastwards, the LIVAS-

697   MIDAS agreement is very good while MERRA-2 DODs are less variable, within the course of the

698   year, with respect to the observed values (Fig. S7-b). Among the three DOD products, a very good

699   temporal agreement it is found in the Thar Desert (Fig. S7-g), but there are deviations regarding the

700   peak of July which is higher in LIVAS (0.88) than in MIDAS (0.75) and MERRA-2 (0.48),

701   respectively. Over downwind continental areas of E. Asia (Fig. S7-i), only few exceptions break down

702   the consistency between MIDAS and LIVAS whereas MERRA-2 is able to reproduce the annual

703   cycle but underestimates the intensity of dust loads. In southern Middle East (Fig. S7-n), the

704   reanalysis and the spaceborne lidar DODs are very well correlated within the course of the year and

705   lower than MIDAS during February-May. In the northern parts (Fig. S7-d), MIDAS gives

706   substantially higher DODs against the well correlated and matched values of LIVAS and MERRA-

707   2. Over the Northern Pacific, Asian dust is transported eastwards during spring affecting nearby (Fig.

708   S7-p) and distant (Fig. S7-j) oceanic areas. The "signal" of this mechanism is clearly evident in

709   MIDAS and MERRA-2 timeseries in contrast to LIVAS, which exhibits substantially lower DOD

710   maxima. Moreover, these maxima appear in the western North Pacific Ocean earlier (March) with

711   respect to the other two datasets (April). Based on MERRA-2 and MIDAS in the sub-Sahel (Fig. S7-

712   o), a primary and a secondary maximum are recorded in March and October, in agreement with

713   ground-based visibility records (N'Tchayi Mbourou et al., 1997). LIVAS reproduces both peaks, but

714   with a weaker intensity in March compared to MIDAS and MERRA-2. However, throughout the

715   year, the maximum LIVAS DOD is observed in June (a local maximum is also recorded in MIDAS),

716   which might be attributed to the strong convection activity favoring the occurrence of haboobs.

717   Saharan dust aerosols, under the impact of the northeasterly harmattan winds, are carried over the

718   Gulf of Guinea (Fig. S7-l) during boreal winter, although DODs among the three datasets reveal a

719   noticeable variability in terms of intensity.

720

721

722

723

4.4. MIDAS DOD global climatology

The annual and seasonal DOD patterns representative for the period 2003 – 2017, are illustrated in Figures 8 and 9, respectively. Among the desert areas of the planet, the most intense dust loads (DODs up to ~1.2; Fig. 8) are observed in the Bodélé Depression located in the northern Lake Chad Basin (Washington et al., 2003). Over the region, these high DODs are sustained throughout the year (Fig. 9) while due the prevailing meteorological conditions, during MAM (Fig. 9-ii) and JJA (Fig. 9-iii), mineral particles are transported westwards, along the Sahel, contributing to the locally emitted anthropogenic dust (Ginoux et al., 2012). Substantial high climatological DODs (up to 0.6; Fig. 8) are recorded in the western sector of Sahara, in contrast to the eastern parts, attributed to the accumulation of dust aerosols primarily in JJA (Fig. 9-iii) and secondarily in MAM (Fig. 9-ii), under the impact of the Saharan Heat Low (Schepanski et al., 2017). Saharan dust is subjected to short-range transport affecting frequently the nearby maritime areas of the Gulf of Guinea (Ben-Ami et al., 2009), the Mediterranean Sea (Gkikas et al., 2015) as well the Red Sea (Banks et al., 2017). Nevertheless, the strongest signal of Saharan dust transport appears over the Tropical Atlantic Ocean with massive loads of mineral particles, confined within the Saharan Air Layer (SAL; Kanitz et al., 2014), reaching the Caribbean Sea (Prospero, 1999), under the impact of the trade winds. The characteristics of the transatlantic dust transport reveal a remarkable intra-annual variation (Fig. 9) as it concerns plumes' latitudinal position, longitudinal extension and intensity, being maximum during boreal summer (Fig. 9-iii).

Dust activity over the Middle East is more pronounced in a "zone" extending from the alluvial plain of the Tigris-Euphrates River to the southern parts of the Arabian Peninsula (Fig. 8), through the eastern flat-lands of Saudi Arabia (Hamidi et al., 2013). Mineral particles emitted from these sources affect also the Persian Gulf (Giannakopoulou and Toumi, 2011) and the Red Sea (Banks et al., 2017); however, the major transport pattern is recorded across the northern Arabian Sea in JJA (Fig. 9-iii), when dust plumes can reach the western coasts of India (Ramaswamy et al., 2018). In the Asian continent, the Taklamakan Desert (Ge et al., 2014), situated in the Tarim basin (NW China), is one of the strongest dust source of the planet yielding DODs up to 1 during spring (Fig. 9-ii). These intensities are substantially higher than those recorded in the Gobi Desert, located eastwards in the same latitudinal band, due to the different composition of the erodible soils (Sun et al., 2013). Midlatitude cyclones propagating eastwards during springtime (Fig. 9-ii) mobilize dust emission from both sources inducing uplifting and subsequently advection of mineral particles towards the continental E. Asia (Yu et al., 2019) as well as over the north Pacific Ocean (Yu et al., 2008) and exceptionally over the United States (Husar et al., 2001). Other hotspots of dust activity in Asia are recorded in the central parts (Li and Sokolik, 2018) and in the Sistan Basin (Alizadeh Choobari et al.,

759   2013). Dust aerosols originating from agricultural activities along the Indus River basin (Ginoux et

760   al., 2012) and natural processes in the Thar Desert (Proestakis et al., 2018) result in the accumulation

761   of mineral particles in the Pakistan-India borders while under favorable meteorological conditions

762   these loads are carried towards the Indo-Gangetic plain mainly during the pre-monsoon season (Dey

763   et al., 2004). In North America, dust production becomes more evident in the southwestern United

764   States and northwest Mexico in regional terms and during spring within the course of the year (Fig.

765   9-ii). However, DODs are mostly lower than 0.2, with few local exceedances, indicating relatively

766   weak dust emission from the natural (Mojave and Sonoran Deserts; Hand et al., 2017) and

767   anthropogenic (Chihuahuan Desert and Southern Great Plains; Hand et al., 2016) dust sources of the

768   region. Between the two hemispheres, there is a clear contrast in DODs, being substantially lower in

769   the S. Hemisphere, attributed to the weaker processes triggering dust emission from the spatially

770   restricted deserts located in S. Africa (Bryant et al., 2007), S. America (Gassó and Torres, 2019) and

771   in the interior parts of Australia (Prospero et al., 2002).

772   In addition to the global climatological DOD pattern in Figure 8-i, the average of the daily DOD

773   uncertainties provided within the dataset (not to be confused with the uncertainty of the average DOD)

774   and the temporal availability of the MIDAS dataset are shown in Figs. 8-ii and -iii, respectively. More

775   than 70% of daily satellite retrievals with respect to the full period are included in the calculation of

776   the mean DODs (Fig. 8-i) over the cloud-free desert areas. Over dust-affected downwind regions the

777   corresponding percentages range from 30 to 60% (Fig. 8-iii). As expected from Eqs. 4 to 7, daily

778   DOD uncertainties (Fig. 8-ii) scale with DOD and reach up to 0.4 on annual average and 0.5 averaged

779   over MAM and JJA (Figure S8) in the regions with strongest DODs.

780

781   **5.   Summary and conclusions**

782

783   In the current study, we presented the MIDAS (ModIs Dust AeroSol) dust optical depth (DOD)

784   dataset, developed via the synergistic implementation of MODIS-Aqua AOD and dust fraction

785   extracted from collocated MERRA-2 reanalysis outputs. The derived fine resolution (0.1° x 0.1°)

786   global dataset between 2003 and 2017 provides DOD both over continental and oceanic areas, in

787   contrast to similar available satellite products restricted over land surfaces (Ginoux et al., 2012), thus

788   making feasible a thorough and consistent description of dust loads not only over the sources but also

789   over downwind regions. Reanalysis datasets, spanning through decades and available at high

790   temporal frequency, can fulfill such tasks; however, their coarser spatial resolution imposes a

791   restriction when investigating mineral loads' features at finer spatial scales. Our developed DOD

792   product aims at complementing existing observational gaps and can be exploited in a variety of

793 studies (e.g., climatology, trends, evaluation of atmospheric-dust models, radiative effects and data
794 assimilation).

795 The core concept of the applied methodology relies on the utilization of MODIS AOD and
796 MERRA-2 dust fraction (MDF) for the derivation of DOD on MODIS swaths. The validity of MDF
797 has been justified through its evaluation against reference values obtained by the LIVAS database.
798 Over dust-abundant areas extending across the "dust belt", MERRA-2 reproduces adequately the
799 magnitude of dust portion as indicated by the calculated primary statistics (bias, FB, FGE) with the
800 maximum underestimations (up to 10%) being observed in Asian deserts. The agreement between
801 MDF and LIVAS is reduced in the main dust regions of N. America and in the S. Hemisphere.
802 Regarding the temporal covariation of the observed and simulated dust portions, over the period 2007-
803 2015, moderate R values (up to 0.5) are computed above the sources, attributed to the high
804 spatiotemporal variability of the emission processes. On the contrary, the correlation increases
805 substantially (up to 0.9) over maritime downwind regions (Tropical Atlantic Ocean, north Pacific
806 Ocean, Arabian Sea, Mediterranean Sea) where the main dust transport pathways are recorded. Apart
807 from the geographical dependency of the level of agreement between MDF and LIVAS dust fraction,
808 we also investigated the impact of the spatial representativeness of the CALIOP observations.
809 Through this analysis, we revealed that for an increasing number of CALIOP L2 profiles (ranging
810 from 1 to 23), that are aggregated for the derivation of the 1° x 1° LIVAS grid cell, the computed
811 metrics converge towards the ideal scores.

812 Finally, the obtained MIDAS DOD was evaluated against AERONET retrievals and compared
813 with LIVAS and MERRA-2 DODs. AERONET observations were processed to minimize the
814 contribution of other aerosol species making also the assumption that dust loads mainly consist of
815 coarse particles (their radii is larger than the defined inflection point). Overall, the agreement between
816 ~10500 MIDAS-AERONET pairs is very high (R=0.89), whereas the satellite DODs are higher by
817 2.7% with respect to the ground-based ones. At station level, the R values are mainly above 0.8 at
818 most sites of the N. Hemisphere (except western US) while they are mostly lower than 0.5 in the S.
819 Hemisphere. Moreover, positive MIDAS-AERONET deviations (up to 0.2) are mainly encountered
820 in N. Africa and Middle East in contrast to negative values (down to -0.14) recorded at the remaining
821 sites. Based on the annual and seasonal global DOD patterns, corresponding to the period 2007-2015,
822 the locations with the maximum DODs are in a good agreement among the three datasets.
823 Nevertheless, in many regions (e.g., Bodélé, sub-Sahel, north Pacific Ocean) there are deviations on
824 the intensity of dust loads, attributed to the inherent weaknesses of DOD derivation techniques based
825 on different approaches. Despite the regional dependency of deviations among the three datasets, the
826 collocated global long-term averaged DOD is very similar (0.029 for LIVAS, 0.031 for MERRA-2
827 and 0.033 for MIDAS) and close to that reported (0.030) in Ridley et al. (2016). In the S. Hemisphere,

828 the corresponding levels are equal to 0.008 for the three datasets, whereas in the N. Hemisphere,

829 LIVAS DODs (0.051) are lower with respect to MIDAS (0.060) and MERRA-2 (0.056).

830 As a demonstration of the MIDAS dataset, a brief discussion about dust load regime at global

831 scale is made by analyzing the annual and seasonal DOD patterns. The most pronounced dust activity

832 recorded in the Bodélé Depression (DODs up to ~1.2), across the Sahel (DODs up to 0.8), in western

833 parts of the Sahara Desert (DODs up to 0.6), in the eastern parts of the Arabian Peninsula (DODs up

834 to ~1), along the Indus river basin (DODs up to 0.8) and in the Taklamakan Desert (DODs up to ~1).

835 On the contrary, the weaker emission mechanisms triggering dust mobilization over the spatially

836 limited sources of Patagonia, South Africa and interior arid areas of Australia do not favor the

837 accumulation of mineral particles at large amounts (DODs up to 0.4 at local hotspots), even during

838 high-dust seasons. Over oceans, the main pathways of long-range dust transport are observed along

839 the tropical Atlantic and the northern Pacific, revealing a remarkable variation, within the course of

840 the year, in terms of intensity, latitudinal position and range. Finally, the Mediterranean and the

841 Arabian Sea are affected by advected dust plumes originating from N. Africa and Middle East,

842 respectively. Based on the performed uncertainty analysis, the MIDAS DOD product is highly

843 reliable over dust rich regions and becomes more uncertain in areas where the existence of dust loads

844 is not frequent.

845 The exploitation of the MIDAS DOD product will be expanded in other studies in preparation or

846 schedule. At present, focus is given on: (i) the DOD climatology over dust sources and downwind

847 regions, (ii) the implementation of the MIDAS dataset in the DA scheme of the MONARCH model

848 (Di Tomaso et al., 2017), (iii) the estimation of dust radiative effects and the associated impacts on

849 solar energy production, in North Africa and Middle East, upgrading the work of Kosmopoulos et al.

850 (2018) and (iv) the analysis of global and regional trends of dust loads.

851

879

880   **Data availability**

881

882   The MIDAS dataset is available at https://react.space.noa.gr/midas/

883

884   **References**

885

886   Ackerman, S. A.: Remote sensing aerosols using satellite infrared observations, J. Geophys. Res.,

887   102, 17069–17079, https://doi.org/10.1029/96JD03066, 1997.

888

889   Alizadeh Choobari, O., Zawar-Reza, P., and Sturman, A.: Low level jet intensification by mineral

890   dust aerosols, Ann. Geophys., 31, 625-632, https://doi.org/10.5194/angeo-31-625-2013, 2013.

891

892   Amiridis, V., Wandinger, U., Marinou, E., Giannakaki, E., Tsekeri, A., Basart, S., Kazadzis, S.,

893   Gkikas, A., Taylor, M., Baldasano, J., and Ansmann, A.: Optimizing CALIPSO Saharan dust

894   retrievals, Atmos. Chem. Phys., 13, 12089-12106, https://doi.org/10.5194/acp-13-12089-2013, 2013.

895

896   Amiridis, V., Marinou, E., Tsekeri, A., Wandinger, U., Schwarz, A., Giannakaki, E., Mamouri, R.,

897   Kokkalis, P., Binietoglou, I., Solomos, S., Herekakis, T., Kazadzis, S., Gerasopoulos, E., Proestakis,

898   E., Kottas, M., Balis, D., Papayannis, A., Kontoes, C., Kourtidis, K., Papagiannopoulos, N., Mona,

899   L., Pappalardo, G., Le Rille, O., and Ansmann, A.: LIVAS: a 3-D multi-wavelength aerosol/cloud

900   database based on CALIPSO and EARLINET, Atmos. Chem. Phys., 15, 7127-7153,

901   https://doi.org/10.5194/acp-15-7127-2015, 2015.

902

903   Anderson, T. L., Wu, Y., Chu, D. A., Schmid, B., Redemann, J., and Dubovik, O.: Testing the MODIS

904   satellite retrieval of aerosol fine-mode fraction, J. Geophys. Res., 110, D18204,

905   doi:10.1029/2005JD005978, 2005.

906

907   Baars, H., Kanitz, T., Engelmann, R., Althausen, D., Heese, B., Komppula, M., Preissler, J., Tesche,

908   M., Ansmann, A., Wandinger, U., Lim, J.-H., Ahn, J. Y., Stachlewska, I. S., Amiridis, V., Marinou,

909   E., Seifert, P., Hofer, J., Skupin, A., Schneider, F., Bohlmann, S., Foth, A., Bley, S., Pfuller, A.,

910   Giannakaki, E., Lihavainen, H., Viisanen, Y., Hooda, R. K., Pereira, S. N., Bortoli, D., Wagner, F.,

911   Mattis, I., Janicka, L., Markowicz, K. M., Achtert, P., Artaxo, P., Pauliquevis, T., Souza, R. A. F.,

912   Sharma, V. P., van Zyl, P. G., Beukes, J. P., Sun, J., Rohwer, E. G., Deng, R., Mamouri, R.-E. and

913   Zamorano, F.: An overview of the first decade of Polly(NET): an emerging network of automated

914   Raman-polarization lidars for continuous aerosol profiling, Atmos. Chem. Phys., 16(8), 5111–5137,

915   doi:10.5194/acp-16-5111-2016, 2016.

916

917   Banks, J. R. and Brindley, H. E.: Evaluation of MSG-SEVIRI mineral dust retrieval products over

918   Africa and the Middle East, Remote Sensing of Environment, 128, 58–73,

919   doi:10.1016/j.rse.2012.07.017, 2013.

920

921   Banks, J. R., Brindley, H. E., Stenchikov, G., and Schepanski, K.: Satellite retrievals of dust aerosol

922   over the Red Sea and the Persian Gulf (2005–2015), Atmos. Chem. Phys., 17, 3987-4003,

923   https://doi.org/10.5194/acp-17-3987-2017, 2017.

924

925   Basart, S., Pérez, C., Cuevas, E., Baldasano, J. M., and Gobbi, G. P.: Aerosol characterization in

926   Northern Africa, Northeastern Atlantic, Mediterranean Basin and Middle East from direct-sun

927   AERONET observations, Atmos. Chem. Phys., 9, 8265–8282, https://doi.org/10.5194/acp-9-8265-

928   2009, 2009.

929

930   Basart, S., Pérez, C., Nickovic, S., Cuevas, E., and Baldasano, J. M.: Development and evaluation of

931   the BSC-DREAM8b dust regional model over Northern Africa, the Mediterranean and the Middle

932   East, Tellus B, 64, 18539, doi:10.3402/tellusb.v64i0.18539, 2012.

933

934 Ben-Ami, Y., Koren, I., and Altaratz, O.: Patterns of North African dust transport over the Atlantic:
935 winter vs. summer, based on CALIPSO first year data, Atmos. Chem. Phys., 9, 7867-7875,
936 https://doi.org/10.5194/acp-9-7867-2009, 2009.

937

938 Benedetti, A., Morcrette, J.-J., Boucher, O., Dethof, A., Engelen, R. J., Fisher, M., Flentje, H.,
939 Huneeus, N., Jones, L., Kaiser, J. W., Kinne, S., Mangold, A., Razinger, M., Simmons, A. J., Suttie,
940 M., and the GEMS-AER team: Aerosol analysis and forecast in the European Centre for Medium-
941 Range Weather Forecasts Integrated Forecast System: 2. Data assimilation, J. Geophys. Res., 114,
942 D13205, doi:10.1029/2008JD011115, 2009.

943

944 Bryant, R. G., Bigg, G. R., Mahowald, N. M., Eckardt, F. D., and Ross S. G.: Dust emission response
945 to climate in southern Africa, J. Geophys, Res, 112, D09207, doi:10.1029/2005JD007025, 2007.

946

947 Buchard, V., da Silva, A. M., Colarco, P. R., Darmenov, A., Randles, C. A., Govindaraju, R., Torres,
948 O., Campbell, J., and Spurr, R.: Using the OMI aerosol index and absorption aerosol optical depth to
949 evaluate the NASA MERRA Aerosol Reanalysis, Atmos. Chem. Phys., 15, 5743–5760,
950 https://doi.org/10.5194/acp15-5743-2015, 2015.

951

952 Buchard, V., Randles, C.A., da Silva, A.M., Darmenov, A., Colarco, P.R., Govindaraju, R., Ferrare,
953 R., Hair, J., Beyersdorf, A.J., Ziemba, L.D. and Yu, H.: The MERRA-2 aerosol reanalysis, 1980
954 onward. Part II: Evaluation and case studies. Journal of Climate, 30, 6851–6872.
955 https://doi.org/10.1175/ JCLI-D-16-0613, 2017.

956

957 Bullard, J. E., Baddock, M., Bradwell, T., Crusius, J., Darlington, E., Gaiero, D., Gassó, S.,
958 Gisladottir, G., Hodgkins, R., McCulloch, R., McKenna-Neuman, C., Mockford, T., Stewart, H., and,
959 Thorsteinsson, T.: High-latitude dust in the Earth system, Rev. Geophys., 54, 447–485,
960 https://doi.org/10.1002/2016RG000518, 2016.

961

962 Burton, S. P., Hair, J. W., Kahnert, M., Ferrare, R. A., Hostetler, C. A., Cook, A. L., Harper, D. B.,
963 Berkoff, T. A., Seaman, S. T., Collins, J. E., Fenn, M. A. and Rogers, R. R.: Observations of the
964 spectral dependence of linear particle depolarization ratio of aerosols using NASA Langley airborne
965 High Spectral Resolution Lidar, Atmos. Chem. Phys., 15(23), 13453–13473, doi:10.5194/acp-15-
966 13453-2015, 2015.

967 Capelle, V., Chédin, A., Pondrom, M., Crevoisier, C., Armante, R., Crépeau, L. and Scott, N. A.:
968 Infrared dust aerosol optical depth retrieved daily from IASI and comparison with AERONET over
969 the period 2007–2016, Remote Sensing of Environment, 206, 15-32,
970 doi.org/10.1016/j.rse.2017.12.008, 2018

972 Chen, S., Huang, J., Kang, L., Wang, H., Ma, X., He, Y., Yuan, T., Yang, B., Huang, Z., and Zhang,
973 G.: Emission, transport, and radiative effects of mineral dust from the Taklimakan and Gobi deserts:
974 comparison of measurements and model results, Atmos. Chem. Phys., 17, 2401-2421,
975 https://doi.org/10.5194/acp-17-2401-2017, 2017.

977 Chin, M., Ginoux, P., Kinne, S., Torres, O., Holben, B. N., Duncan, D. N., Martin, R. V., Logan, J.
978 A., Higurashi, H., and Nakajima, T.: Tropospheric aerosol optical thickness from the GOCART
979 model and comparisons with satellite and Sun photometer measurements, J. Atmos. Sci., 59, 451–
980 483, https://doi.org/10.1175/1520-0469(2002)059<0461:TAOTFT>2.0.CO;2, 2002.

982 Clarisse, L., Clerbaux, C., Franco, B., Hadji-Lazaro, J., Whitburn, S., Kopp, A. K., et al.: A decadal
983 data set of global atmospheric dust retrieved from IASI satellite measurements, Journal of
984 Geophysical Research: Atmospheres, 124, https://doi.org/10.1029/2018JD029701, 2019.

986 Colarco, P., da Silva, A., Chin, M., and Diehl, T.: Online simulations of global aerosol distributions
987 in the NASA GEOS-4 model and comparisons to satellite and ground-based aerosol optical depth, J.
988 Geophys. Res., 115, D14207, https://doi.org/10.1029/2009JD012820, 2010.

990 Colarco, P. R., Nowottnick, E. P., Randles, C. A., Yi, B., Yang, P., Kim, K.-M., Smith, J. A., and
991 Bardeen, C. G.: Impact of radiatively interactive dust aerosols in the NASA GEOS-5 climate model:
992 Sensitivity to dust particle shape and refractive index, J. Geophys. Res.-Atmos., 119, 753–786,
993 https://doi.org/10.1002/2013JD020046, 2014.

995 Dey, S., Tripathi, S. N., Singh, R. P., and Holben, B. N.: Influence of dust storms on the aerosol
996 optical properties over the Indo-Gangetic basin, J. Geophys. Res.-Atmos., 109, 1–10,
997 doi:10.1029/2004jd004924, 2004.

999 Di Tomaso, E., Schutgens, N. A. J., Jorba, O., and Pérez García-Pando, C.: Assimilation of MODIS
1000 Dark Target and Deep Blue observations in the dust aerosol component of NMMB-MONARCH
1001 version 1.0, Geosci. Model Dev., 10, 1107-1129, https://doi.org/10.5194/gmd-10-1107-2017, 2017.

1002

1003 Diehl, T., Heil, A., Chin, M., Pan, X., Streets, D., Schultz, M., and Kinne, S.: Anthropogenic, biomass
1004 burning, and volcanic emissions of black carbon, organic carbon, and SO2 from 1980 to 2010 for
1005 hindcast model experiments, Atmos. Chem. Phys. Discuss., 12, 24895–24954,
1006 https://doi.org/10.5194/acpd-12-24895- 2012, 2012.

1007
1008 Du, Y., Xu, X., Chu, M., Guo, Y., and Wang, J.: Air particulate matter and cardiovascular disease:
1009 the epidemiological, biomedical and clinical evidence, J. Thorac. Dis., 8, E8,
1010 https://doi.org/10.3978/j.issn.2072-1439.2015.11.37, 2016.

1011
1012 Dubovik, O. and King, M. D.: A flexible inversion algorithm for retrieval of aerosol optical properties
1013 from Sun and sky radiance measurements, J. Geophys. Res., 105, 20673–
1014 20696,https://doi.org/10.1029/2000JD900282, 2000.

1015
1016 Dubovik, O., Sinyuk, A., Lapyonok, T., Holben, B. N., Mishchenko, M., Yang, P., Eck, T. F., Volten,
1017 H., Munoz, O., Veihelmann, B., and Van der Zande, W. J.: Application of spheroid models to account
1018 for aerosol particle nonsphericity in remote sensing of desert dust, J. Geophys. Res.-Atmos., 111,
1019 D11208, https://doi.org/10.1029/2005JD006619, 2006.

1020
1021 Ekström, M., McTainsh, G. H. and Chappell, A.: Australian dust storms: temporal trends and
1022 relationships with synoptic pressure distributions (1960–99), Int. J. Climatol., 24, 1581–1599,
1023 doi:10.1002/joc.1072, 2004.

1024
1025 Engelstaedter, S., Tegen, I., and Washington, R.: North African dust emissions and transport, Earth-
1026 Sci. Rev., 79, 73–100, https://doi.org/10.1016/j.earscirev.2006.06.004, 2006.

1027
1028 Fiedler, S., Schepanski, K., Heinold, B., Knippertz, P., and Tegen, I.: Climatology of nocturnal low-
1029 level jets over North Africa and implications for modeling mineral dust emission, J. Geophys. Res.-
1030 Atmos., 118, 6100–6121, 2013.

1031
1032 Flaounas, E., Kotroni, V., Lagouvardos, K., Kazadzis, S., Gkikas, A., and Hatzianastassiou, N.:
1033 Cyclone contribution to dust transport over the Mediterranean region, Atmos. Sci. Lett., 16, 473–478,
1034 doi:10.1002/asl.584, 2015.

1035

1036 Fotiadi, A., Hatzianastassiou, N., Drakakis, E., Matsoukas, C., Pavlakis, K. G., Hatzidimitriou, D.,
1037 Gerasopoulos, E., Mihalopoulos, N., and Vardavas, I.: Aerosol physical and optical properties in the
1038 Eastern Mediterranean Basin, Crete, from Aerosol Robotic Network data, Atmos. Chem. Phys., 6,
1039 5399-5413, https://doi.org/10.5194/acp-6-5399-2006, 2006.

1041 Freudenthaler, V., Esselborn, M., Wiegner, M., Heese, B., Tesche, M., Ansmann, A., Mueller, D.,
1042 Althausen, D., Wirth, M., Fix, A., Ehret, G., Knippertz, P., Toledano, C., Gasteiger, J., Garhammer,
1043 M. and Seefeldner, A.: Depolarization ratio profiling at several wavelengths in pure Saharan dust
1044 during SAMUM 2006, Tellus Ser. B-Chem. Phys. Meteorol., 61(1), 165–179, doi:10.1111/j.1600-
1045 0889.2008.00396.x, 2009.

1047 Gassó, S., & Torres, O.: Temporal characterization of dust activity in the Central Patagonia desert
1048 (years 1964–2017), Journal of Geophysical Research: Atmospheres, 124, 3417– 3434,
1049 https://doi.org/10.1029/2018JD030209.

1051 Ge, J. M., Huang, J. P., Xu, C. P., Qi, Y. L., and Liu, H. Y.: Characteristics of Taklimakan dust
1052 emission and distribution: a satellite and reanalysis field perspective, J. Geophys. Res.-Atmos., 119,
1053 11772–11783, https://doi.org/10.1002/2014JD022280, 2014.

1055 Gelaro, R, McCarty, W., Suárez, M. J., Todling, R., Molod, A., Takacs, L., Randles, C. A., Darmenov,
1056 A., Bosilovich, M. G., Reichle, R., Wargan, K., Coy, L., Cullather, R., Draper, C., Akella, S.,
1057 Buchard, V., Conaty, A., da Silva, A. M., Gu, W., Kim, G., Koster, R., Lucchesi, R., Merkova, D.,
1058 Nielsen, J. E., Partyka, G., Pawson, S., Putman, W., Rienecker, M., Schubert, S. D., Sienkiewicz, M.,
1059 and Zhao, B.: The Modern-Era Retrospective Analysis for Research and Applications, Version 2
1060 (MERRA-2), J. Climate, 30, 5419–5454, https://doi.org/10.1175/JCLI-D-16-0758.1, 2017.

1062 Georgoulias, A. K., Alexandri, G., Kourtidis, K. A., Lelieveld, J., Zanis, P., Pöschl, U., Levy, R.,
1063 Amiridis, V., Marinou, E., and Tsikerdekis, A.: Spatiotemporal variability and contribution of
1064 different aerosol types to the aerosol optical depth over the Eastern Mediterranean, Atmos. Chem.
1065 Phys., 16, 13853-13884, doi:10.5194/acp-16-13853-2016, 2016.

1067 Georgoulias, A. K., Tsikerdekis, A., Amiridis, V., Marinou, E., Benedetti, A., Zanis, P., Alexandri,
1068 G., Mona, L., Kourtidis, K. A. and Lelieveld, J.: A 3-D evaluation of the MACC reanalysis dust
1069 product over Europe, northern Africa and Middle East using CALIOP/CALIPSO dust satellite
1070 observations, Atmos. Chem. Phys., 18(12), 8601–8620, doi:10.5194/acp-18-8601-2018, 2018.

1071

1072   Giannakopoulou, E. M. and Toumi, R.: The Persian Gulf summertime low-level jet over sloping

1073   terrain, Q. J. Roy. Meteor. Soc., 138, 145–157, doi:10.1002/qj.901, 2011.

1074

1075   Giles, D. M., Holben, B. N., Eck, T. F., Sinyuk, A., Smirnov, A., Slutsker, I., Dickerson, R. R.,

1076   Thompson, A. M., and Schafer, J. S.: An analysis of AERONET aerosol absorption properties and

1077   classifications representative of aerosol source regions, J. Geophys. Res., 117, D17203,

1078   https://doi.org/10.1029/2012JD018127, 2012.

1079

1080   Giles, D. M., Sinyuk, A., Sorokin, M. G., Schafer, J. S., Smirnov, A., Slutsker, I., Eck, T. F., Holben,

1081   B. N., Lewis, J. R., Campbell, J. R., Welton, E. J., Korkin, S. V., and Lyapustin, A. I.: Advancements

1082   in the Aerosol Robotic Network (AERONET) Version 3 database – automated near-real-time quality

1083   control algorithm with improved cloud screening for Sun photometer aerosol optical depth (AOD)

1084   measurements, Atmos. Meas. Tech., 12, 169–209, https://doi.org/10.5194/amt-12-169-2019, 2019.

1085

1086   Ginoux, P., Chin, M., Tegen, I., Prospero, J. M., Holben, B., Dubovik, O., and Lin, S. J.: Sources and

1087   distributions of dust aerosols simulated with the GOCART model, J. Geophys. Res.-Atmos., 106,

1088   20255–20273, https://doi.org/10.1029/2000jd000053, 2001.

1089

1090   Ginoux, P., Prospero, J. M., Torres, O., and Chin, M.: Longterm simulation of global dust distribution

1091   with the GOCART model: correlation with North Atlantic Oscillation, Environ. Modell. Softw., 19,

1092   113–128, https://doi.org/10.1016/S1364- 8152(03)00114-2, 2004.

1093

1094   Ginoux, P., Prospero, J. M., Gill, T. E., Hsu, N. C., and Zhao, M.: Global-scale attribution of

1095   anthropogenic and natural dust sources and their emission rates based on MODIS Deep Blue aerosol

1096   products, Rev. Geophys., 50, RG3005, https://doi.org/10.1029/2012RG000388, 2012.

1097

1098   Gkikas, A., Hatzianastassiou, N., Mihalopoulos, N., Katsoulis, V., Kazadzis, S., Pey, J., Querol, X.,

1099   and Torres, O.: The regime of intense desert dust episodes in the Mediterranean based on

1100   contemporary satellite observations and ground measurements, Atmos. Chem. Phys., 13, 12135-

1101   12154, https://doi.org/10.5194/acp-13-12135-2013, 2013.

1102

1103   Gkikas, A., Houssos, E. E., Lolis, C. J., Bartzokas, A., Mihalopoulos, N., and Hatzianastassiou, N.:

1104   Atmospheric circulation evolution related to desert-dust episodes over the Mediterranean, Q. J. Roy.

1105   Meteor. Soc., 141, 1634–1645, doi:10.1002/qj.2466, 2015.

1106

1107 Gkikas, A., Basart, S., Hatzianastassiou, N., Marinou, E., Amiridis, V., Kazadzis, S., Pey, J., Querol,

1108 X., Jorba, O., Gassó, S., and Baldasano, J. M.: Mediterranean intense desert dust outbreaks and their

1109 vertical structure based on remote sensing data, Atmos. Chem. Phys., 16, 8609-8642,

1110 https://doi.org/10.5194/acp-16-8609-2016, 2016.

1111

1112 Gkikas, A., Obiso, V., Pérez García-Pando, C., Jorba, O., Hatzianastassiou, N., Vendrell, L., Basart,

1113 S., Solomos, S., Gassó, S., and Baldasano, J. M.: Direct radiative effects during intense Mediterranean

1114 desert dust outbreaks, Atmos. Chem. Phys., 18, 8757-8787, https://doi.org/10.5194/acp-18-8757-

1115 2018, 2018.

1116

1117 Gkikas, A., Giannaros, T.M., Kotroni, V., Lagouvardos, K.: Assessing the radiative impacts of an

1118 extreme desert dust outbreak and the potential improvements on short-term weather forecasts: The

1119 case of February 2015, Atmos. Res., 226, 152-170, https://doi.org/10.1016/j.atmosres.2019.04.020,

1120 2019.

1121

1122 Gong, S. L.: A parameterization of sea-salt aerosol source function for sub- and super-micron

1123 particles, Global Biogeochem. Cy., 17, 1097, https://doi.org/10.1029/2003GB002079, 2003.

1124

1125 Hamidi, M., Kavianpour, M. R., and Shao, Y.: Synoptic analysis of dust storms in the Middle East,

1126 Asia-Pac. J. Atmos. Sci., 49, 279–286, 2013.

1127

1128 Hand, J. L., White, W. H., Gebhart, K. A., Hyslop, N. P., Gill, T. E., and Schichtel, B. A.: Earlier

1129 onset of the spring fine dust season in the southwestern United States, Geophys. Res. Lett., 43, 4001–

1130 4009, https://doi.org/10.1002/2016gl068519, 2016.

1131

1132 Hand, J. L., Gill, T. E., and Schichtel, B. A.: Spatial and seasonal variability in fine mineral dust and

1133 coarse aerosol mass at re-mote sites across the United States, J. Geophys. Res.-Atmos.,122, 3080–

1134 3097, https://doi.org/10.1002/2016jd026290, 2017.

1135

1136 Haustein, K., Pérez, C., Baldasano, J. M., Jorba, O., Basart, S., Miller, R. L., Janjic, Z., Black, T.,

1137 Nickovic, S., Todd, M. C., Washington, R., Müller, D., Tesche, M., Weinzierl, B., Esselborn, M., and

1138 Schladitz, A.: Atmospheric dust modeling from meso to global scales with the online NMMB/BSC-

1139 Dust model – Part 2: Experimental campaigns in Northern Africa, Atmos. Chem. Phys., 12, 2933-

1140 2958, https://doi.org/10.5194/acp-12-2933-2012, 2012.

Haywood, J. and Boucher, O.: Estimates of the direct and indirect radiative forcing due to tropospheric aerosols: A review, Rev. Geophys., 38, 513–543, https://doi.org/10.1029/1999RG000078, 2000.

Hess, M., Koepke, P., and Schult, I.: Optical Properties of Aerosols and Clouds: The Software Package OPAC, B. Am. Meteorol. Soc., 79, 831–844, https://doi.org/10.1175/1520-0477(1998)0792.0.CO;2, 1998.

Holben, B. N., Eck, T. F., Slutsker, I., Tanre, D., Buis, J. P., Setzer, A., Vermote, E., Reagan, J. A., Kaufman, Y., Nakajima, T., Lavenue, F., Jankowiak, I., and Smirnov, A.: AERONET – A federated instrument network and data archive for aerosol characterization, Remote Sens. Environ., 66, 1–16, https://doi.org/10.1016/S0034-4257(98)00031-5, 1998.

Hsu, N. C., Tsay, S. C., King, M. D., and Herman, J. R.: Aerosol Properties Over Bright-Reflecting Source Regions, IEEE T. Geosci. Remote, 42, 557–569, doi:10.1109/TGRS.2004.824067, 2004.

Hubanks, P. A., Platnick, S., King, M., and Ridgway, R.: MODIS Atmosphere L3 Gridded Product Algorithm Theoretical Basis Document (ATBD) & Users Guide, ATBD Reference Number: L3_ATBD_C6_2018_04_11, 2018.

Hunt, W. H., Winker, D. M., Vaughan, M. A., Powell, K. A., Lucker, P. L. and Weimer, C.: CALIPSO Lidar Description and Performance Assessment, J. Atmos. Oceanic Technol., 26(7), 1214–1228, doi:10.1175/2009JTECHA1223.1, 2009.

Hussain, A., Mir, H., Afzal, M.: Analysis of dust storms frequency over Pakistan during (1961–2000), Pakistan J. Meteorol., 2(3): 49–68, 2005.

Husar, R. B., Tratt, D. M., Schichtel, D. M., Falke, S. R., Li, F., Jaffe, D., Gassó, S., Gill, T., Laulainen, N. S., Lu, F., Reheis, M. C., Chun, Y., Westphal, D., Holben, B. N., Gueymard, C., McKendry, I., Kuring, N., Feldman, G. C., McClain, C., Frouin, R. J., Merrill, J., DuBois, D., Vignola, F., Murayama, T., Nickovic, S., Wilson, W. E., Sassen, K., Sugimoto, N., and Malm, W. C.: Asian dust events of April 1998, J. Geophys. Res., 106, 18317–18330, https://doi.org/10.1029/2000JD900788, 2001.

1176　Hyer, E. J., Reid, J. S., and Zhang, J.: An over-land aerosol optical depth data set for data assimilation
1177　by filtering, correction, and aggregation of MODIS Collection 5 optical depth retrievals, Atmos.
1178　Meas. Tech., 4, 379-408, https://doi.org/10.5194/amt-4-379-2011, 2011.

1179

1180　Inness, A., Baier, F., Benedetti, A., Bouarar, I., Chabrillat, S., Clark, H., Clerbaux, C., Coheur, P.,
1181　Engelen, R. J., Errera, Q., Flemming, J., George, M., Granier, C., Hadji-Lazaro, J., Huijnen, V.,
1182　Hurtmans, D., Jones, L., Kaiser, J. W., Kapsomenakis, J., Lefever, K., Leitão, J., Razinger, M.,
1183　Richter, A., Schultz, M. G., Simmons, A. J., Suttie, M., Stein, O., Thépaut, J.-N., Thouret, V.,
1184　Vrekoussis, M., Zerefos, C., and the MACC team: The MACC reanalysis: an 8 yr data set of
1185　atmospheric composition, Atmos. Chem. Phys., 13, 4073–4109, https://doi.org/10.5194/acp13-4073-
1186　2013, 2013.

1187

1188　Inness, A., Ades, M., Agustí-Panareda, A., Barré, J., Benedictow, A., Blechschmidt, A.-M.,
1189　Dominguez, J. J., Engelen, R., Eskes, H., Flemming, J., Huijnen, V., Jones, L., Kipling, Z., Massart,
1190　S., Parrington, M., Peuch, V.-H., Razinger, M., Remy, S., Schulz, M., and Suttie, M.: The CAMS
1191　reanalysis of atmospheric composition, Atmos. Chem. Phys., 19, 3515–3556,
1192　https://doi.org/10.5194/acp-19-3515-2019, 2019.

1193

1194　Jickells, T. D., An, Z. S., Andersen, K. K., Baker, A. R., Bergametti, G., Brooks, N., Cao, J. J., Boyd,
1195　P. W., Duce, R. A., Hunter, K. A., Kawahata, H., Kubilay, N., laRoche, J., Liss, P. S., Mahowald, N.,
1196　Prospero, J. M., Ridgwell, A. J., Tegen, I., and Torres, R.: Global iron connections between desert
1197　dust, ocean biogeochemistry, and climate, Science, 308, 67–71, 2005.

1198

1199　Kanakidou, M., Mihalopoulos, N., Kindap, T., Im, U., Vrekoussis, M., Gerasopoulos, E., Dermitzaki,
1200　E., Unal, A., Kocak, M., Markakis, K., Melas, D., Kouvarakis, G., Youssef, A. F., Richter, A.,
1201　Hatzianastassiou, N., Hilboll, A., Ebojie, F., Wittrock, F., von Savigny, C., Burrows, J. P.,
1202　Ladstaetter-Weissenmayer, A., and Moubasher, H.: Megacities as hot spots of air pollution in the
1203　East Mediterranean, Atmos. Environ., 45, 1223–1235,
1204　https://doi.org/10.1016/j.atmosenv.2010.11.048, 2011.

1205

1206　Kanatani, K.T., Ito, I., Al-Delaimy, W.K., Adachi, Y., Mathews, W.C., Ramsdell, J.W.: Toyama
1207　Asian Desert Dust and Asthma Study Group Members. Desert dust exposure is associated with
1208　increased risk of asthma hospitalization in children, Am. J. Respir. Crit. Care Med. 182 (12),
1209　1475e1481. https://doi.org/10. 1164/rccm.201002-0296OC, 2010.

1210

1211 Kanitz, T., Engelmann, R., Heinold, B., Baars, H., Skupin, A., and Ansmann, A.: Tracking the
1212 Saharan Air Layer with shipborne lidar across the tropical Atlantic, Geophys. Res. Lett., 41, 1044–
1213 1050, doi:10.1002/2013GL058780, 2014.

1214

1215 Kaufman, Y. J., Koren, I., Remer, L. A., Tanré, D., Ginoux, P., and Fan, S.: Dust transport and
1216 deposition observed from the Terra-Moderate Resolution Imaging Spectroradiometer (MODIS)
1217 spacecraft over the Atlantic Ocean, J. Geophys. Res.-Atmos., 110, 1–16,
1218 https://doi.org/10.1029/2003JD004436, 2005.

1219

1220 Kergoat, L., Guichard, F., Pierre, C., and Vassal, C.: Influence of dry-season vegetation variability
1221 on Sahelian dust during 2002–2015, Geophys. Res. Lett., 44, 5231–5239,
1222 https://doi.org/10.1002/2016GL072317, 2017.

1223

1224 Kim, D., Chin, M., Yu, H., Eck, T. F., Sinyuk, A., Smirnov, A., and Holben, B. N.: Dust optical
1225 properties over North Africa and Arabian Peninsula derived from the AERONET dataset, Atmos.
1226 Chem. Phys., 11, 10733-10741, https://doi.org/10.5194/acp-11-10733-2011, 2011.

1227

1228 Kittaka, C., Winker, D. M., Vaughan, M. A., Omar, A., and Remer, L. A.: Intercomparison of column
1229 aerosol optical depths from CALIPSO and MODIS-Aqua, Atmos. Meas. Tech., 4, 131– 141,
1230 https://doi.org/10.5194/amt-4-131-2011, 2011.

1231

1232 Klingmüller, K., Pozzer, A., Metzger, S., Stenchikov, G. L., and Lelieveld, J.: Aerosol optical depth
1233 trend over the Middle East, Atmos. Chem. Phys., 16, 5063-5073, https://doi.org/10.5194/acp-16-
1234 5063-2016, 2016.

1235

1236 Klose, M. and Shao, Y.: Stochastic parameterization of dust emission and application to convective
1237 atmospheric conditions, Atmos. Chem. Phys., 12, 7309-7320, https://doi.org/10.5194/acp-12-7309-
1238 2012, 2012.

1239

1240 Knippertz, P., Deutscher, C., Kandler, K., Müller, T., Schulz, O., and Schütz, L.: Dust mobilization
1241 due to density currents in the Atlas region: Observations from the Saharan Mineral Dust Experiment
1242 2006 field campaign, J. Geophys. Res.-Atmos., 112, 1–14, https://doi.org/10.1029/2007JD008774,
1243 2007.

1244

1245 Koch, J. and Renno, N. O.: The role of convective plumes and vortices on the global aerosol budget,

1246 Geophys. Res. Lett., 32, L18806, doi:10.1029/2005GL023420, 2005.

1247

1248 Konsta, D., Binietoglou, I., Gkikas, A., Solomos, S., Marinou, E., Proestakis, E., Basart, S., Pérez

1249 García-Pando, C., El-Askary, H., Amiridis, V.: Evaluation of the BSC-DREAM8b regional dust

1250 model using the 3D LIVAS-CALIPSO, Atmos. Environ., 195, 46-62,

1251 https://doi.org/10.1016/j.atmosenv.2018.09.047, 2018.

1252

1253 Kosmopoulos, P. G., Kazadzis, S., Taylor, M., Athanasopoulou, E., Speyer, O., Raptis, P. I., Marinou,

1254 E., Proestakis, E., Solomos, S., Gerasopoulos, E., Amiridis, V., Bais, A. and Kontoes, C.: Dust impact

1255 on surface solar irradiance assessed with model simulations, satellite observations and ground-based

1256 measurements, Atmos. Meas. Tech., 10(7), doi:10.5194/amt-10-2435-2017, 2017.

1257

1258 Kosmopoulos, P.G., Kazadzis, S., El-Askary, H., Taylor, M., Gkikas, A., Proestakis, E., Kontoes, C.,

1259 El-Khayat, M.M.: Earth-Observation-Based Estimation and Forecasting of Particulate Matter Impact

1260 on Solar Energy in Egypt, Remote Sens., 10, 1870, 2018.

1261

1262 Lambert, F., Kug, J.-S., Park, R. J., Mahowald, N., Winckler, G., Abe-Ouchi, A., O'ishi, R.,

1263 Takemura, T., and Lee, J.-H.: The role of mineral-dust aerosols in polar temperature amplification,

1264 Nat. Clim. Change, 3, 487–491, https://doi.org/10.1038/nclimate1785, 2013.

1265

1266 Levy, R. C., Remer, L. A., and Dubovik, O.: Global aerosol optical properties and application to

1267 Moderate Resolution Imaging Spectroradiometer aerosol retrieval over land, J. Geophys. Res.-

1268 Atmos., 112, D13210, doi:10.1029/2006JD007815, 2007a.

1269

1270 Levy, R. C., Remer, L. A., Mattoo, S., Vermote, E. F., and Kaufman, Y. J.: Second-generation

1271 operational algorithm: Retrieval of aerosol properties over land from inversion of Moderate

1272 Resolution Imaging Spectroradiometer spectral reflectance, J. Geophys. Res.-Atmos., 112, D13211,

1273 doi:10.1029/2006JD007811, 2007b.

1274

1275 Levy, R. C., Leptoukh, G. G., Kahn, R., Zubko, V., Gopalan, A., and Remer, L. A.: A critical look at

1276 deriving monthly aerosol optical depth from satellite data, IEEE Transactions on Geoscience and

1277 Remote Sensing, 47, 2942–2956, https://doi.org/10.1109/TGRS.2009.2013842, 25 2009.

1278

1279 Levy, R. C., Remer, L. A., Kleidman, R. G., Mattoo, S., Ichoku, C., Kahn, R., and Eck, T. F.: Global
1280 evaluation of the Collection 5 MODIS dark-target aerosol products over land, Atmos. Chem. Phys.,
1281 10, 10399–10420, doi:10.5194/acp-10-10399-2010, 2010.

1283 Levy, R. C., Mattoo, S., Munchak, L. A., Remer, L. A., Sayer, A. M., Patadia, F., and Hsu, N. C.:
1284 The Collection 6 MODIS aerosol products over land and ocean, Atmos. Meas. Tech., 6, 2989–3034,
1285 https://doi.org/10.5194/amt-6-2989-2013, 2013.

1287 Li, W., El-Askary, H., Qurban, M. A, Proestakis E., Garay M. J., Kalashnikova, O. V., Amiridis, V.,
1288 Gkikas, A., Marinou, E., Piechota, T. and ManiKandan, K. P.: An Assessment of Atmospheric and
1289 Meteorological Factors Regulating Red Sea Phytoplankton Growth, Remote Sens., 10(5), 673;
1290 doi:10.3390/rs10050673, 2018.

1292 Li, L., and Sokolik, I.: Analysis of Dust Aerosol Retrievals Using Satellite Data in Central Asia,
1293 Atmosphere, 9, 288, 2018.

1295 Liu, D., Wang, Z., Liu, Z., Winker, D., and Trepte, C.: A height resolved global view of dust aerosols
1296 from the first year CALIPSO lidar measurements, J. Geophys. Res.-Atmos., 113, D16214,
1297 https://doi.org/10.1029/2007JD009776, 2008.

1299 Liu, D., Taylor, J. W., Crosier, J., Marsden, N., Bower, K. N., Lloyd, G., Ryder, C. L., Brooke, J. K.,
1300 Cotton, R., Marenco, F., Blyth, A., Cui, Z., Estelles, V., Gallagher, M., Coe, H., and Choularton, T.
1301 W.: Aircraft and ground measurements of dust aerosols over the west African coast in summer 2015
1302 during ICE-D and AER-D, Atmos. Chem. Phys., 18, 3817-3838, https://doi.org/10.5194/acp-18-
1303 3817-2018, 2018.

1305 Lynch, P., Reid, J. S., Westphal, D. L., Zhang, J., Hogan, T. F., Hyer, E. J., Curtis, C. A., Hegg, D.
1306 A., Shi, Y., Campbell, J. R., Rubin, J. I., Sessions, W. R., Turk, F. J., and Walker, A. L.: An 11-year
1307 global gridded aerosol optical thickness reanalysis (v1.0) for atmospheric and climate sciences,
1308 Geosci. Model Dev., 9, 1489-1522, https://doi.org/10.5194/gmd-9-1489-2016, 2016.

1310 Ma, X., Bartlett, K., Harmon, K., and Yu, F.: Comparison of AOD between CALIPSO and MODIS:
1311 significant differences over major dust and biomass burning regions, Atmos. Meas. Tech., 6, 2391-
1312 2401, https://doi.org/10.5194/amt-6-2391-2013, 2013.

1314   Mamouri, R. E. and Ansmann, A.: Fine and coarse dust separation with polarization lidar, Atmos.
1315   Meas. Tech., 7, 3717-3735, https://doi.org/10.5194/amt-7-3717-2014, 2014.

1316

1317   Mamouri, R.-E. and Ansmann, A.: Potential of polarization/Raman lidar to separate fine dust, coarse
1318   dust, maritime, and anthropogenic aerosol profiles, Atmos. Meas. Tech., 10(9), 3403–3427,
1319   doi:10.5194/amt-10-3403-2017, 2017.

1320

1321   Marinou, E., Amiridis, V., Binietoglou, I., Tsikerdekis, A., Solomos, S., Proestakis, E., Konsta, D.,
1322   Papagiannopoulos, N., Tsekeri, A., Vlastou, G., Zanis, P., Balis, D., Wandinger, U., and Ansmann,
1323   A.: Three-dimensional evolution of Saharan dust transport towards Europe based on a 9-year
1324   EARLINET-optimized CALIPSO dataset, Atmos. Chem. Phys., 17, 5893-5919,
1325   https://doi.org/10.5194/acp-17-5893-2017, 2017.

1326

1327   McCarty, W., Coy, L., Gelaro, R., Huang, A., Merkova, D., Smith, E. B., Sienkiewicz, M., and
1328   Wargan, K.: MERRA-2 input observations: Summary and initial assessment. Technical Report Series
1329   on Global Modeling and Data Assimilation, Vol. 46, NASA Tech. Rep. NASA/TM–2016–104606,
1330   61 pp., 2016. [Available online at https://gmao.gsfc.nasa.gov/pubs/docs/ McCarty885.pdf.]

1331

1332   Meng, Z. K., Yang, P., Kattawar, G. W., Bi, L., Liou, K. N., and Laszlo, I.: Single-scattering
1333   properties of tri-axial ellipsoidal mineral dust aerosols: A database for application to radiative transfer
1334   calculations, J. Aerosol Sci., 41, 501–512, https://doi.org/10.1016/j.jaerosci.2010.02.008, 2010.

1335

1336   Middleton, N. J. and Goudie, A. S.: Saharan dust: sources and trajectories, T. I. Brit. Geogr., 26, 165–
1337   181, doi:10.1111/1475- 5661.00013, 2001.

1338

1339   Molod, A., Takacs, L., Suarez, M., and Bacmeister, J.: Development of the GEOS-5 atmospheric
1340   general circulation model: evolution from MERRA to MERRA2, Geosci. Model Dev., 8, 1339-1356,
1341   https://doi.org/10.5194/gmd-8-1339-2015, 2015.

1342

1343   Mukkavilli, S.K., Prasad, A.A., Taylor, R.A., Huang, J., Troccoli, A., Kay, M.J.: Assessment of
1344   atmospheric aerosols from two reanalysis products over Australia, Atmos. Res., 215, 149-164, 2019.

1345

1346   Müller, D., Ansmann, A., Mattis, I., Tesche, M., Wandinger, U., Althausen, D., and Pisani, G.:
1347   Aerosol-type-dependent lidar ratios observed with Raman lidar, J. Geophys. Res.-Atmos., 112,
1348   https://doi.org/10.1029/2006JD008292, 2007.

1349

1350 Nabat, P., Somot, S., Mallet, M., Michou, M., Sevault, F., Driouech, F., Meloni, D., di Sarra, A., Di
1351 Biagio, C., Formenti, P., Sicard, M., Léon, J.-F., and Bouin, M.-N.: Dust aerosol radiative effects
1352 during summer 2012 simulated with a coupled regional aerosol–atmosphere–ocean model over the
1353 Mediterranean, Atmos. Chem. Phys., 15, 3303-3326, https://doi.org/10.5194/acp-15-3303-2015,
1354 2015.

1355

1356 N'Tchayi Mbourou, G., Berrand, J. J., and Nicholson, S. E.: The diurnal and seasonal cycles of wind-
1357 borne dust over Africa north of the equator, J. Appl. Meteorol., 36, 868–882, 1997.

1358

1359 Okin, G. S., Mahowald, N., Chadwick, O. A., and Artaxo, P.: Impact of desert dust on the
1360 biogeochemistry of phosphorus in terrestrial ecosystems, Global Biogeochem. Cy., 18, GB2005,
1361 https://doi.org/10.1029/2003GB002145, 2004.

1362

1363 Omar, A. H., Winker, D. M., Vaughan, M. A., Hu, Y., Trepte, C. R., Ferrare, R. A., Lee, K. P.,
1364 Hostetler, C. A., Kittaka, C., Rogers, R. R., and Kuehn, R. E.: The CALIPSO Automated Aerosol
1365 Classification and Lidar Ratio Selection Algorithm, J. Atmos. Ocean. Tech., 26, 1994–2014,
1366 https://doi.org/10.1175/2009JTECHA1231.1, 2009.

1367

1368 Omar, A. H., Winker, D. M., Tackett, J. L., Giles, D. M., Kar, J., Liu, Z., Vaughan, M. A., Powell,
1369 K. A., and Trepte, C. R., CALIOP and AERONET aerosol optical depth comparisons: One size fits
1370 none, J. Geophys. Res.-Atmos., 118, 4748–4766, https://doi.org/10.1002/jgrd.50330, 2013.

1371

1372 O'Neill, N. T., Eck, T. F., Smirnov, A., Holben, B. N., and Thulasiraman, S.: Spectral discrimination
1373 of coarse and fine mode optical depth, J. Geophys. Res., 108, 4559–4573,
1374 https://doi.org/10.1029/2002JD002975, 2003.

1375

1376 Pease, P. P., Tchakerian, V. P., and Tindale, N. W.: Aerosols over the Arabian Sea: geochemistry and
1377 source areas for Aeolian desert dust, J. Arid Environ., 39, 477–496,
1378 https://doi.org/10.1006/jare.1997.0368, 1998.

1379

1380 Pérez, C., Nickovic, S., Pejanovic, G., Baldasano, J. M., and Özsoy, E.: Interactive dust-radiation
1381 modeling: A step to improve weather forecasts, J. Geophys. Res., 111, 1–17, 2006.

1382

1383 Pérez, C., Haustein, K., Janjic, Z., Jorba, O., Huneeus, N., Baldasano, J. M., Black, T., Basart, S.,
1384 Nickovic, S., Miller, R. L., Perlwitz, J. P., Schulz, M., and Thomson, M.: Atmospheric dust modeling
1385 from meso to global scales with the online NMMB/BSC-Dust model – Part 1: Model description,
1386 annual simulations and evaluation, Atmos. Chem. Phys., 11, 13001-13027,
1387 https://doi.org/10.5194/acp-11-13001-2011, 2011.

1389 Pérez García-Pando, C., Stanton, M. C., Diggle, P. J., Trzaska, S., Miller, R. L., Perlwitz, J. P.,
1390 Baldasano, J. M., Cuevas, E., Ceccato, P., Yaka, P., and Thomson, M. C.: Soil Dust Aerosols and
1391 Wind as Predictors of Seasonal Meningitis Incidence in Niger, Environ. Health Perspect., 122, 679–
1392 686, doi:10.1289/ehp.1306640, 2014.

1394 Peyridieu, S., Chédin, A., Capelle, V., Tsamalis, C., Pierangelo, C., Armante, R., Crevoisier, C.,
1395 Crépeau, L., Siméon, M., Ducos, F., and Scott, N. A.: Characterisation of dust aerosols in the infrared
1396 from IASI and comparison with PARASOL, MODIS, MISR, CALIOP, and AERONET observations,
1397 Atmos. Chem. Phys., 13, 6065-6082, https://doi.org/10.5194/acp-13-6065-2013, 2013.

1399 Proestakis, E., Amiridis, V., Marinou, E., Georgoulias, A. K., Solomos, S., Kazadzis, S., Chimot, J.,
1400 Che, H., Alexandri, G., Binietoglou, I., Daskalopoulou, V., Kourtidis, K. A., de Leeuw, G., and van
1401 der A, R. J.: Nine-year spatial and temporal evolution of desert dust aerosols over South and East
1402 Asia as revealed by CALIOP, Atmos. Chem. Phys., 18, 1337-1362, https://doi.org/10.5194/acp-18-
1403 1337-2018, 2018.

1405 Prospero, J. M.: Long-range transport of mineral dust in the global atmosphere: Impact of African
1406 dust on the environment of the southeastern United States, P. Natl. Acad. Sci. USA, 96, 3396–3403,
1407 1999.

1409 Prospero, J. M., Ginoux, P., Torres, O., Nicholson, S. E., and Gill, T. E.: Environmental
1410 characterization of global sources of atmospheric soil dust identified with the Nimbus 7 Total Ozone
1411 Mapping Spectrometer (TOMS) absorbing aerosol product, Rev. Geophys., 40, 2-1–2-31, 2002.

1413 Prospero, J. M. and Mayol-Bracero, O. L.: Understanding the transport and impact of African dust
1414 on the Caribbean Basin, B. Am. Meteorol. Soc., 94, 1329–1335, 2013.

1416 Querol, X., Tobías, A., Pérez, N., Karanasiou, A., Amato, F., Stafoggia, M., Pérez García-Pando, C.,
1417 Ginoux, P., Forastiere, F., Gumy, S., P., Alastuey, A.: Monitoring the impact of desert dust outbreaks

for air quality for health studies, Environment International, 130, 104867, 2019. https://doi.org/10.1016/j.envint.2019.05.061.

Ramaswamy, V.P., Muraleedharan, M., Prakash Babu, C.: Mid-troposphere transport of Middle-East dust over the Arabian Sea and its effect on rainwater composition and sensitive ecosystems over India. Scientific Reports 7, 13676, https://doi.org/10.1038/s41598-017-13652-1, 2018.

Rashki, A., Kaskaoutis, D.G., Francois, P., Kosmopoulos, P.G., Legrand, M.: Dust-storm dynamics over Sistan region, Iran: seasonality, transport characteristics and affected areas, Aeol. Res., 16, 35–48, 2015.

Reid, J. S., Reid, E. A., Walker, A., Piketh, S., Cliff, S., Al Mandoos, A., Tsay, S.-C., and Eck, T. F.: Dynamics of southwest Asian dust particle size characteristics with implications for global dust research, J. Geophys. Res., 113, D14212, https://doi.org/10.1029/2007JD009752, 2008.

Remer, L. A., Tanre, D., Kaufman, Y. J., Ichoku, C., Mattoo, S., Levy, R., Chu, D. A., Holben, B., Dubovik, O., Smirnov, A., Martins, J. V., Li, R. R., and Ahmad, Z.: Validation of MODIS aerosol retrieval over ocean, Geophys. Res. Lett., 29, MOD3.1–MOD3.4, doi:10.1029/2001GL013204, 2002.

Remer, L. A., Kaufman, Y. J., Tanre, D., Mattoo, S., Chu, D. A., Martins, J. V., Li, R. R., Ichoku, C., Levy, R. C., Kleidman, R. G., Eck, T. F., Vermote, E., and Holben, B. N.: The MODIS aerosol algorithm, products, and validation, J. Atmos. Sci., 62, 947–973, doi:10.1175/JAS3385.1, 2005.

Remer, L. A., Kleidman, R. G., Levy, R. C., Kaufman, Y. J., Tanré, D., Mattoo, S., Martins, J. V., Ichoku, C., Koren, I., Yu, H. and Holben, B. N.: Global aerosol climatology from the MODIS satellite sensors, J. Geophys. Res.-Atmos., 113, D14S07, doi:10.1029/2007JD009661, 2008.

Ridley, D. A., Heald, C. L., Kok, J. F., and Zhao, C.: An observationally constrained estimate of global dust aerosol optical depth, Atmos. Chem. Phys., 16, 15097–15117, https://doi.org/10.5194/acp-16-15097-2016, 2016.

Rienecker, M. M., Suarez, M. J., Todling, R., Bacmeister, J., Takacs, L., Liu, H. C., Gu, W., Sienkiewicz, M., Koster, R. D., Gelaro, R., Stajner, I., and Nielsen, J. E.: The GEOS-5 Data Assimilation System-Documentation of Versions 5.0.1, 5.1.0, and 5.2.0 Technical Report Series on Global Modeling and Data Assimilation, v27, 2008.

1452

Rodríguez, S., Alastuey, A., and Querol, X.: A review of methods for long term in situ characterization of aerosol dust, Aeolian Res., 6, 55–74, doi:10.1016/j.aeolia.2012.07.004, 2012.

Sayer, A. M., Hsu, N. C., Bettenhausen, C., and Jeong, M.-J.: Validation and uncertainty estimates for MODIS Collection 6 "Deep Blue" aerosol data, J. Geophys. Res., 118, 7864–7873, https://doi.org/10.1002/jgrd.50600, 2013.

Sayer, A. M., Munchak, L. A., Hsu, N. C., Levy, R. C., Bettenhausen, C., and Jeong, M.-J.: MODIS Collection 6 aerosol products: comparison between aqua's e-deep blue, dark target, and "merged" data sets, and usage recommendations, J. Geophys. Res.-Atmos., 119, 13965–13989, doi:10.1002/2014JD022453, 2014.

Schepanski, K., Tegen, I., Laurent, B., Heinold, B., and Macke, A.: A new Saharan dust source activation frequency map derived from MSG-SEVIRI IR-channels, Geophys. Res. Lett., 34, L18803, https://doi.org/10.1029/2007GL030168, 2007.

Schepanski, K., Tegen, I., and Macke, A.: Comparison of satellite based observations of Saharan dust source areas, Remote Sensing of Environment, 123, 90–97, http://www.sciencedirect.com/science/article/pii/S0034425712001381, 2012.

Schepanski, K., Heinold, B., and Tegen, I.: Harmattan, Saharan heat low, and West African monsoon circulation: modulations on the Saharan dust outflow towards the North Atlantic, Atmos. Chem. Phys., 17, 10223-10243, https://doi.org/10.5194/acp-17-10223-2017, 2017.

Schepanski, K.: Transport of Mineral Dust and Its Impact on Climate, Geosciences, 8, https://doi.org/10.3390/geosciences8050151, 2018.

Schuster, G. L., Vaughan, M., MacDonnell, D., Su, W., Winker, D., Dubovik, O., Lapyonok, T., and Trepte, C.: Comparison of CALIPSO aerosol optical depth retrievals to AERONET measurements, and a climatology for the lidar ratio of dust, Atmos. Chem. Phys., 12, 7431-7452, https://doi.org/10.5194/acp-12-7431-2012, 2012.

1484

Shi, Y., Zhang, J., Reid, J. S., Holben, B., Hyer, E. J., and Curtis, C.: An analysis of the collection 5 MODIS over-ocean aerosol optical depth product for its implication in aerosol assimilation, Atmos. Chem. Phys., 11, 557-565, https://doi.org/10.5194/acp-11-557-2011, 2011.

Sinyuk, A., Holben, B. N., Eck, T. F., Giles, D. M., Slutsker, I., Korkin, S., Schafer, J. S., Smirnov, A., Sorokin, M., and Lyapustin, A.: The AERONET Version 3 aerosol retrieval algorithm, associated uncertainties and comparisons to Version 2, Atmos. Meas. Tech., 13, 3375–3411, https://doi.org/10.5194/amt-13-3375-2020, 2020.

Sokolik, I. N. and Toon, O. B.: Direct radiative forcing by anthropogenic airborne mineral aerosols, Nature, 381, 681–683, https://doi.org/10.1038/381681a0, 1996.

Solomos, S., Kalivitis, N., Mihalopoulos, N., Amiridis, V., Kouvarakis, G., Gkikas, A., Binietoglou, I., Tsekeri, A., Kazadzis, S., Kottas, M., Pradhan, Y., Proestakis, E., Nastos, P. T. and Marenco, F.: From Tropospheric Folding to Khamsin and Foehn Winds: How Atmospheric Dynamics Advanced a Record-Breaking Dust Episode in Crete, Atmosphere, 9(7), 240, doi:10.3390/atmos9070240, 2018.

Stefanski, R. and Sivakumar, M. V. K.: Impacts of sand and dust storms on agriculture and potential agricultural applications of a SDSWS, IOP Conf. Ser.: Earth Environ. Sci., 7, 012016, doi: 10.1088/1755-1307/7/1/012016, 2009.

Stephens, G. L., Vane, D. G., Boain, R. J., Mace, G. G., Sassen, K., Wang, Z. E., Illingworth, A. J., O'Connor, E. J., Rossow, W. B., Durden, S. L., Miller, S. D., Austin, R. T., Benedetti, A. and Mitrescu, C.: The cloudsat mission and the a-train - A new dimension of space-based observations of clouds and precipitation, Bull. Amer. Meteorol. Soc., 83(12), 1771–1790, doi:10.1175/BAMS-83-12-1771, 2002.

Su, L. and Toon, O. B.: Saharan and Asian dust: similarities and differences determined by CALIPSO, AERONET, and a coupled climate-aerosol microphysical model, Atmos. Chem. Phys., 11, 3263-3280, https://doi.org/10.5194/acp-11-3263-2011, 2011.

Sun, Y., Chen, H., Tada, R., Weiss, D., Lin, M., Toyoda, S., Yan, Y., and Isozaki, Y.: ESR signal intensity and crystallinity of quartz from Gobi and sandy deserts in East Asia and implication for tracing Asian dust provenance, Geochem. Geophy. Geosy., 14, 2615–2627, https://doi.org/10.1002/ggge.20162, 2013.

Sun, E., Xu, X., Che, H., Tang, Z., Gui, K., An, L., Lu, C., and Shi, G.: Variation in MERRA-2 aerosol optical depth and absorption aerosol optical depth over China from 1980 to 2017, J. Atmos. Sol.-Terr. Phys., 186, 8–19, https://doi.org/10.1016/j.jastp.2019.01.019, 2019.

Tackett, J. L., Winker, D. M., Getzewich, B. J., Vaughan, M. A., Young, S. A. and Kar, J.: CALIPSO lidar level 3 aerosol profile product: version 3 algorithm design, Atmos. Meas. Tech., 11(7), 4129–4152, doi:10.5194/amt-11-4129-2018, 2018.

Tafuro, A. M., Barnaba, F., De Tomasi, F., Perrone, M. R., and Gobbi, G. P.: Saharan dust particle properties over the central Mediterranean, Atmos. Res., 81, 67–93, 2006.

Tesche, M., Ansmann, A., Müller, D., Althausen, D., Engelmann, R., Freudenthaler, V., and Grob, S.: Vertically Resolved Separation of Dust and Smoke over Cape Verde Using Multiwavelength Raman and Polarization Lidars during Saharan Mineral Dust Experiment 2008, J. Geophys. Res., 114, D13202, doi:10.1029/2009JD011862, 2009.

Textor, C., Schulz, M., Guibert, S., Kinne, S., Balkanski, Y., Bauer, S., Berntsen, T., Berglen, T., Boucher, O., Chin, M., Dentener, F., Diehl, T., Easter, R., Feichter, H., Fillmore, D., Ghan, S., Ginoux, P., Gong, S., Grini, A., Hendricks, J., Horowitz, L., Huang, P., Isaksen, I., Iversen, I., Kloster, S., Koch, D., Kirkevåg, A., Kristjansson, J. E., Krol, M., Lauer, A., Lamarque, J. F., Liu, X., Montanaro, V., Myhre, G., Penner, J., Pitari, G., Reddy, S., Seland, Ø., Stier, P., Takemura, T., and Tie, X.: Analysis and quantification of the diversities of aerosol life cycles within AeroCom, Atmos. Chem. Phys., 6, 1777-1813, https://doi.org/10.5194/acp-6-1777-2006, 2006.

Toledano, C., Cachorro, V. E., Berjon, A., De Frutos, A. M., Sorribas, M., De la Morena, B. A., and Goloub, P.: Aerosol optical depth and Ångström exponent climatology at El Arenosillo AERONET site (Huelva, Spain), Q. J. Roy. Meteor. Soc., 133, 795–807, 2007.

Torres, O., Bhartia, P. K., Herman, J. R., Ahmad, Z., and Gleason, J.: Derivation of aerosol properties from satellite measurements of backscattered ultraviolet radiation: Theoretical basis, J. Geophys. Res., 103, 17099–17110, https://doi.org/10.1029/98JD00900, 1998.

Torres, O., Bhartia, P. K., Jethva, H., and Ahn, C.: Impact of the ozone monitoring instrument row anomaly on the long-term record of aerosol products, Atmos. Meas. Tech., 11, 2701-2715, https://doi.org/10.5194/amt-11-2701-2018, 2018.

Tsikerdekis, A., Zanis, P., Steiner, A. L., Solmon, F., Amiridis, V., Marinou, E., Katragkou, E., Karacostas, T., and Foret, G.: Impact of dust size parameterizations on aerosol burden and radiative forcing in RegCM4, Atmos. Chem. Phys., 17, 769–791, https://doi.org/10.5194/acp-17-769-2017, 2017.

Vandenbussche, S., Kochenova, S., Vandaele, A. C., Kumps, N., and De Mazière, M.: Retrieval of desert dust aerosol vertical profiles from IASI measurements in the TIR atmospheric window, Atmos. Meas. Tech., 6, 2577–2591, https://doi.org/10.5194/amt-6-2577-2013, 2013.

Vandenbussche, S., Callewaert, S., Schepanski, K., and De Mazière, M.: North African mineral dust sources: new insights from a combined analysis based on 3D dust aerosols distributions, surface winds and ancillary soil parameters, Atmos. Chem. Phys. Discuss., https://doi.org/10.5194/acp-2020-130, in review, 2020.

Vaughan, M. A., Powell, K. A., Kuehn, R. E., Young, S. A., Winker, D. M., Hostetler, C. A., Hunt, W. H., Liu, Z., McGill, M. J. and Getzewich, B. J.: Fully Automated Detection of Cloud and Aerosol Layers in the CALIPSO Lidar Measurements, J. Atmos. Ocean. Technol., 26(10), 2034–2050, doi:10.1175/2009JTECHA1228.1, 2009.

Veselovskii, I., Goloub, P., Podvin, T., Tanre, D., da Silva, A., Colarco, P., Castellanos, P., Korenskiy, M., Hu, Q., Whiteman, D. N., Pérez-Ramírez, D., Augustin, P., Fourmentin, M., and Kolgotin, A.: Characterization of smoke and dust episode over West Africa: comparison of MERRA-2 modeling with multiwavelength Mie–Raman lidar observations, Atmos. Meas. Tech., 11, 949-969, https://doi.org/10.5194/amt-11-949-2018, 2018.

Vickery, K. J., Eckardt, F. D., and Bryant, R. G.: A sub-basin scale dust plume source frequency inventory for south-ern Africa, 2005–2008, Geophys. Res. Lett., 40, 5274–5279, doi:10.1002/grl.50968, 2013.

1586 Voss, K. K., and Evan, A. T.: A new satellite-based global climatology of dust aerosol optical depth.
1587 Journal of Applied Meteorology and Climatology, doi:10.1175/jamc-d-19-0194.1, 2020.

1588

1589 Wandinger, U., Tesche, M., Seifert, P., Ansmann, A., Müller, D., and Althausen, D.: Size matters:
1590 Influence of multiple scattering on CALIPSO light-extinction profiling in desert dust, Geophys. Res.
1591 Lett., 37, L10801, doi:10.1029/2010GL042815, 2010.

1592 Washington, R., Todd, M., Middleton, N. J., and Goudie, A. S.: Dust-storm source areas determined
1593 by the total ozone monitoring spectrometer and surface observations, Ann. Assoc. Am. Geogr., 93,
1594 297–313, https://doi.org/10.1111/1467-8306.9302003, 2003.

1595

1596 Wei, J., Peng, Y., Mahmood, R., Sun, L., and Guo, J.: Intercomparison in spatial distributions and
1597 temporal trends derived from multi-source satellite aerosol products, Atmos. Chem. Phys., 19, 7183–
1598 7207, https://doi.org/10.5194/acp-19-7183-2019, 2019a.

1599

1600 Wei, J., Li, Z., Peng, Y., and Sun, L.: MODIS Collection 6.1 aerosol optical depth products over land
1601 and ocean: validation and comparison, Atmos. Environ., 201, 428–440, 2019b.

1602

1603 Weinzierl, B., Sauer, D., Minikin, A., Reitebuch, O., Dahlkotter, F., Mayer, B., Emde, C., Tegen, I.,
1604 Gasteiger, J., Petzold, A., Veira, A., Kueppers, U., and Schumann, U.: On the visibility of airborne
1605 volcanic ash and mineral dust from the pilot's perspective in flight, Phys Chem Earth, 45-46, 87-102,
1606 10.1016/j.pce.2012.04.003, 2012.

1607

1608 Winker, D. M., Vaughan, M. A., Omar, A., Hu, Y., Powell, K. A., Liu, Z., Hunt, W. H. and Young,
1609 S. A.: Overview of the CALIPSO Mission and CALIOP Data Processing Algorithms, J. Atmos.
1610 Oceanic Technol., 26(11), 2310–2323, doi:10.1175/2009JTECHA1281.1, 2009.

1611

1612 Winker, D. M., Pelon, J., Coakley, J. A., Ackerman, S. A., Charlson, R. J., Colarco, P. R., Flamant,
1613 P., Fu, Q., Hoff, R. M., Kittaka, C., Kubar, T. L., Le Treut, H., McCormick, M. P., Megie, G., Poole,
1614 L., Powell, K., Trepte, C., Vaughan, M. A. and Wielicki, B. A.: THE CALIPSO MISSION A Global
1615 3D View of Aerosols and Clouds, Bull. Amer. Meteorol. Soc., 91(9), 1211–1229,
1616 doi:10.1175/2010BAMS3009.1, 2010.

1617

1618 Wu, W. S., Purser, R. J., and Parrish, D. F.: Three-dimensional variational analysis with spatially
1619 inhomogeneous covariances, Mon. Weather Rev., 130, 2905–2916, doi:10.1175/1520-
1620 0493(2002)130 2.0.Co;2, 2002.

1621

1622 Yu, H., Remer, L. A., Chin, M., Bian, H., Kleidman, R. G., and Diehl, T.: A satellite-based assessment
1623 of transpacific transport of pollution aerosol, J. Geophys. Res.-Atmos., 113, D14S12,
1624 https://doi.org/10.1029/2007JD009349, 2008.

1625

1626 Yu, H. B., Chin, M., Winker, D. M., Omar, A. H., Liu, Z. Y., Kittaka, C., and Diehl, T.: Global view
1627 of aerosol vertical distributions from CALIPSO lidar measurements and GOCART simulations:
1628 Regional and seasonal variations, J. Geophys. Res.-Atmos., 115, D00H30,
1629 https://doi.org/10.1029/2009jd013364, 2010.

1630

1631 Yu, H. B., Chin, M., Yuan, T. L., Bian, H. S., Remer, L. A., Prospero, J. M., Omar, A., Winker, D.,
1632 Yang, Y. K., Zhang, Y., Zhang, Z. B., and Zhao, C.: The fertilizing role of African dust in the Amazon
1633 rainforest: A first multiyear assessment based on data from Cloud-Aerosol Lidar and Infrared
1634 Pathfinder Satellite Observations, Geophys. Res. Lett., 42, 1984–1991,
1635 https://doi.org/10.1002/2015gl063040, 2015.

1636

1637 Yu, S., Eder, B., Dennis, R., Chu, S. H., and Schwartz, S. E.: New unbiased symmetric metrics for
1638 evaluation of air quality models, Atmos. Sci. Lett., 7, 26–34, 2006.

1639

1640 Yu, Y., Notaro, M., Liu, Z., Kalashnikova, O., Alkolibi, F., Fadda, E., and Bakhrjy, F.: Assessing
1641 temporal and spatial variations in atmospheric dust over Saudi Arabia through satellite, radiometric,
1642 and station data, J. Geophys. Res.-Atmos., 118, 13253– 13264,
1643 https://doi.org/10.1002/2013JD020677, 2013.

1644

1645 Yu, Y., Kalashnikova, O. V., Garay, M. J., and Notaro, M.: Climatology of Asian dust activation and
1646 transport potential based on MISR satellite observations and trajectory analysis, Atmos. Chem. Phys.,
1647 19, 363-378, https://doi.org/10.5194/acp-19-363-2019, 2019.

1648

1649 Zender, C. S., Huisheng, B., and Newman, D.: Mineral Dust Entrainment and Deposition (DEAD)
1650 model: Description and 1990s dust climatology, J. Geophys. Res., 108, 4416,
1651 https://doi.org/10.1029/2002JD002775, 2003.

1652

1653 Zender, C. S., Miller, R. L. L., and Tegen, I.: Quantifying mineral dust mass budgets: Terminology,

1654 constraints, and current estimates, Eos, Transactions American Geophysical Union, 85, 509–512,

1655 https://doi.org/10.1029/2004EO480002, 2011.

1656

1657 Zhang, J. and Reid, J. S.: MODIS aerosol product analysis for data assimilation: Assessment of over-

1658 ocean level 2 aerosol optical thickness retrievals, J. Geophys. Res.-Atmos., 111, D22207,

1659 https://doi.org/10.1029/2005JD006898, 2006.

1660

1661 **Table 1:** Planetary (GLB), hemispherical (NHE and SHE) and regional DOD averages representative for the period 2007-

1662 2015, based on collocated LIVAS, MERRA-2 and MIDAS 1°x1° data. Within the brackets are given the minimum and

1663 maximum annual values. The regional averages have been calculated following the upper branch (first temporal averaging

1664 and then spatial averaging) in Figure 5 of Levy et al. (2009). The full names of the acronyms for each sub-region are

1665 given in the caption of Figure 7.

1666

REGION	LIVAS	MERRA-2	MIDAS
GLB	0.029 [0.028 – 0.035]	0.031 [0.028 – 0.036]	0.033 [0.031 – 0.040]
NHE	0.051 [0.050 – 0.064]	0.056 [0.050 – 0.067]	0.060 [0.056 – 0.074]
SHE	0.008 [0.007 – 0.008]	0.008 [0.007 – 0.008]	0.008 [0.007 – 0.008]
ETA	0.107 [0.085 – 0.175]	0.096 [0.079 – 0.143]	0.110 [0.089 – 0.167]
WTA	0.027 [0.022 – 0.034]	0.019 [0.016 – 0.024]	0.022 [0.018 – 0.029]
MED	0.074 [0.061 – 0.096]	0.089 [0.079 – 0.105]	0.097 [0.085 – 0.110]
GOG	0.164 [0.085 – 0.303]	0.275 [0.077 – 0.440]	0.326 [0.098 – 0.512]
WSA	0.271 [0.241 – 0.341]	0.339 [0.315 – 0.383]	0.325 [0.291 – 0.439]
SSA	0.287 [0.236 – 0.390]	0.260 [0.158 – 0.350]	0.249 [0.160 – 0.353]
BOD	0.302 [0.211 – 0.366]	0.510 [0.393 – 0.633]	0.612 [0.415 – 0.896]
NME	0.252 [0.121 – 0.305]	0.265 [0.148 – 0.295]	0.360 [0.201 – 0.397]
SME	0.236 [0.177 – 0.277]	0.220 [0.181 – 0.288]	0.257 [0.199 – 0.346]
CAS	0.077 [0.047 – 0.091]	0.140 [0.129 – 0.207]	0.146 [0.109 – 0.185]
THA	0.169 [0.115 – 0.197]	0.138 [0.113 – 0.150]	0.125 [0.080 – 0.155]
TAK	0.362 [0.284 – 0.429]	0.259 [0.236 – 0.322]	0.140 [0.099 – 0.290]
GOB	0.105 [0.076 – 0.140]	0.118 [0.105 – 0.138]	0.139 [0.066 – 0.141]
EAS	0.088 [0.053 – 0.127]	0.065 [0.048 – 0.080]	0.074 [0.055 – 0.089]
WNP	0.015 [0.012 – 0.020]	0.027 [0.021 – 0.030]	0.029 [0.023 – 0.032]
ENP	0.008 [0.006 – 0.010]	0.019 [0.016 – 0.020]	0.020 [0.017 – 0.023]
SUS	0.021 [0.011 – 0.031]	0.028 [0.019 – 0.038]	0.020 [0.013 – 0.025]

1667

(i)

(ii)
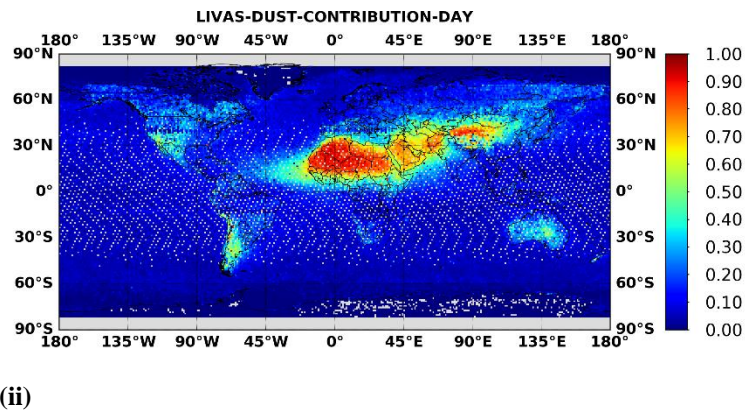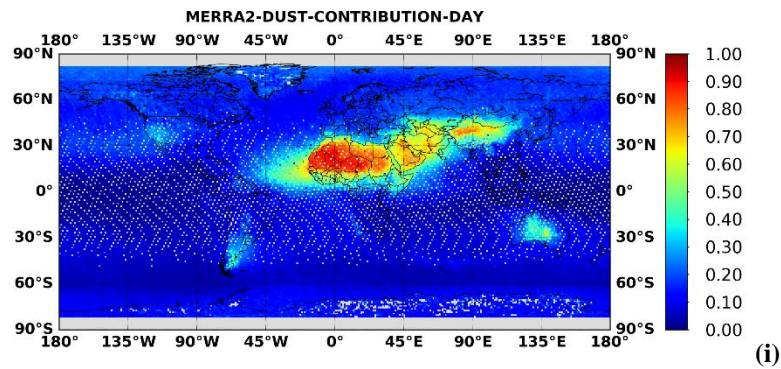
1668 **Figure 1:** Annual geographical distributions of dust contribution to total aerosol optical depth at 1° x 1° spatial resolution
1669 based on **(i)** MERRA-2 at 550 nm and **(ii)** LIVAS at 532 nm, during daytime conditions, over the period 2007-2015.
1670

(i)

(ii)

(iii)

(iv)
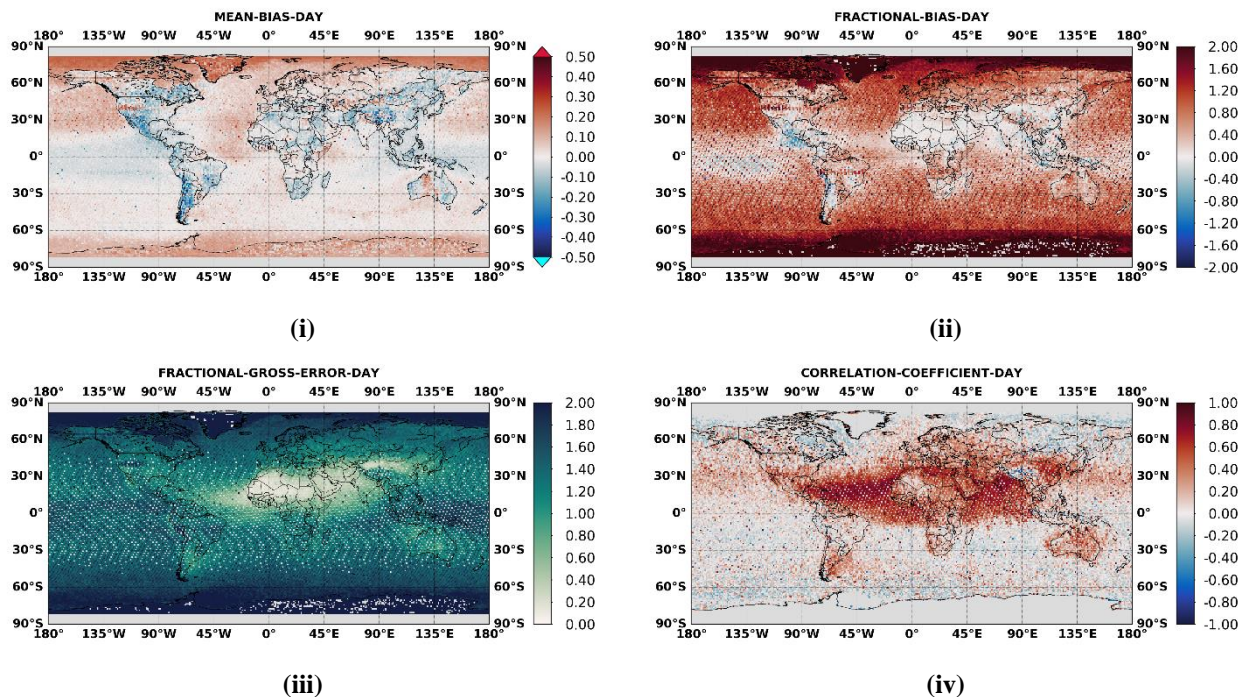
1671 **Figure 2:** Annual geographical distributions illustrating the assessment of MDF versus LIVAS dust fraction, during
1672 daytime conditions at 1° x 1° spatial resolution, according to the primary skill metrics of: **(i)** mean bias, **(ii)** fractional
1673 bias, **(iii)** fractional gross error and **(iv)** correlation coefficient, representative for the period 2007-2015.
1674

MIDAS (2003-2017)

(i)

MIDAS-DOD (2003-2017)

(ii)
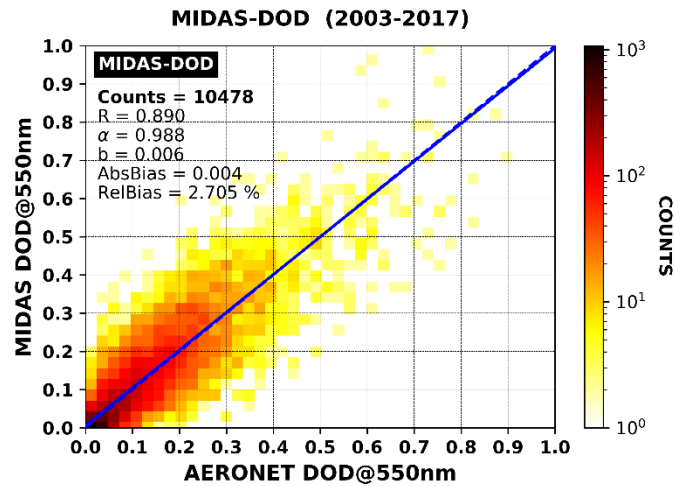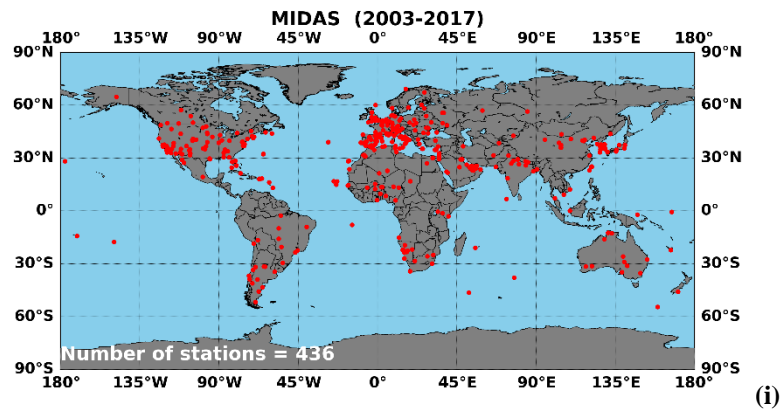
Figure 3: **(i)** AERONET sites where at least one pair of ground-based and spaceborne retrievals has been recorded according to the defined collocation criteria during the period 2003 – 2017. **(ii)** Density scatterplot between MIDAS (y-axis) and AERONET (x-axis) dust optical depth at 550nm. The solid and dashed lines stand for the linear regression fit and equal line (y=x), respectively.
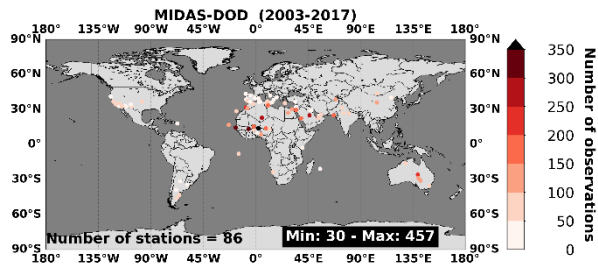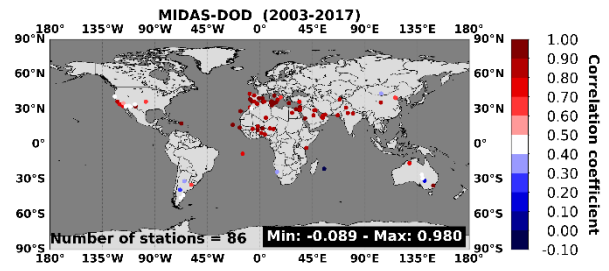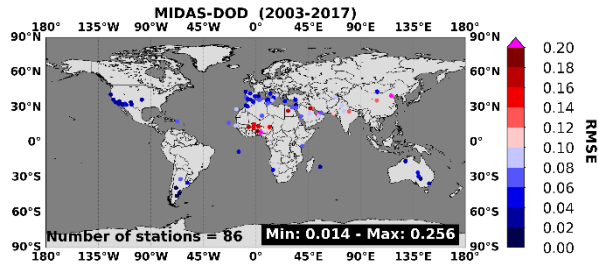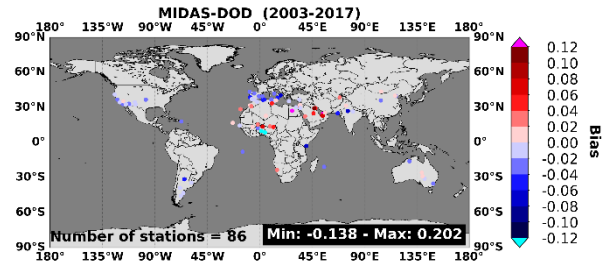
Figure 4: Scatterplot metrics between MIDAS and AERONET DOD$_{550nm}$, at station level, during the period 2003 – 2017.
(i) Number of concurrent MIDAS-AERONET observations, **(ii)** correlation coefficient, **(iii)** root mean square error and
(iv) bias defined as spaceborne minus ground-based retrievals. The obtained scores are presented only for sites with at
least 30 MIDAS-AERONET matchups.

LIVAS-DOD
ANNUAL (2007-2015)

(i)

MERRA2-DOD
ANNUAL (2007-2015)

(ii)

MIDAS-DOD
ANNUAL (2007-2015)

(iii)
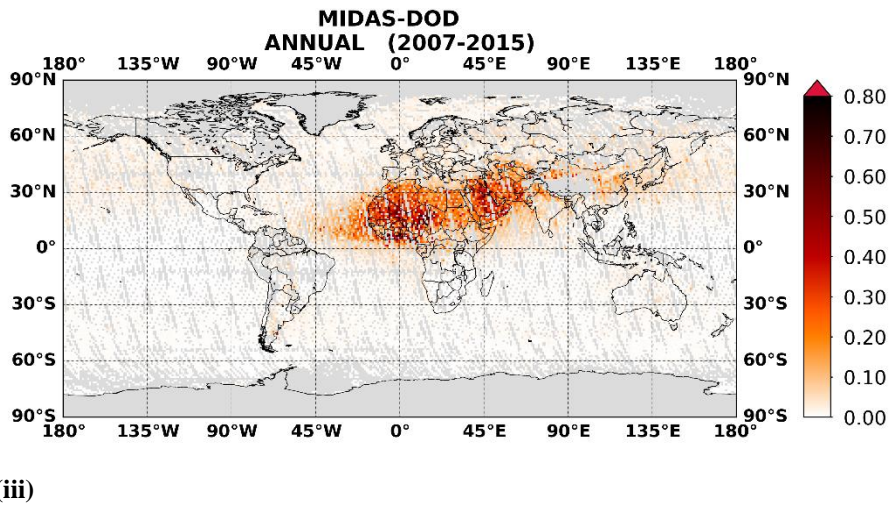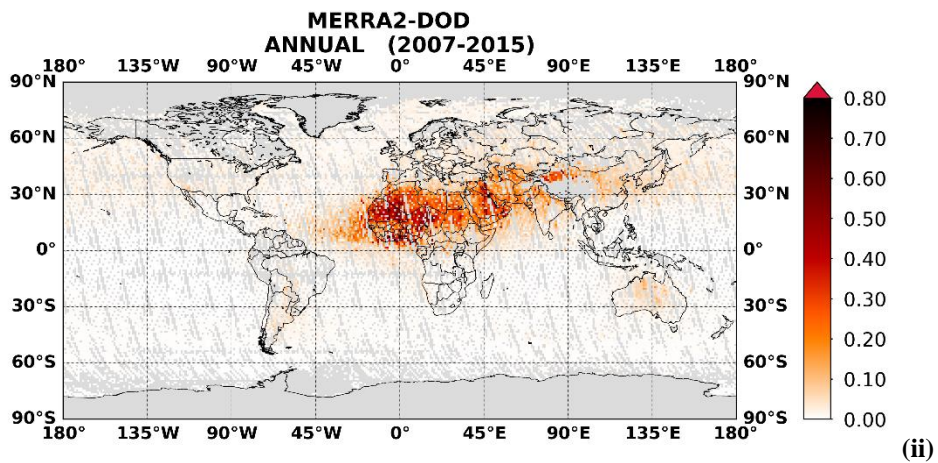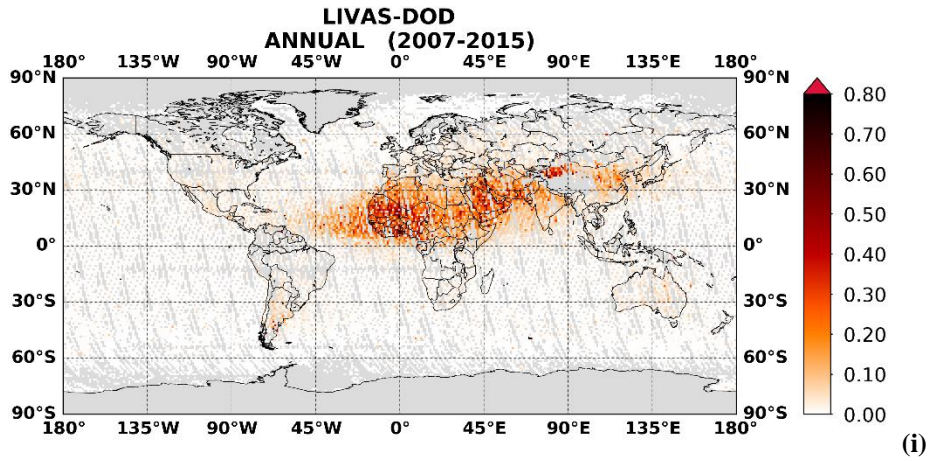
Figure 5: Long-term (2007 – 2015) average geographical collocated distributions at 1° x 1° spatial resolution during daytime for: **(i)** LIVAS DOD_{532nm}, **(ii)** MERRA-2 DOD_{550nm} and **(iii)** MIDAS DOD_{550nm}.

(i)

(ii)

(iii)
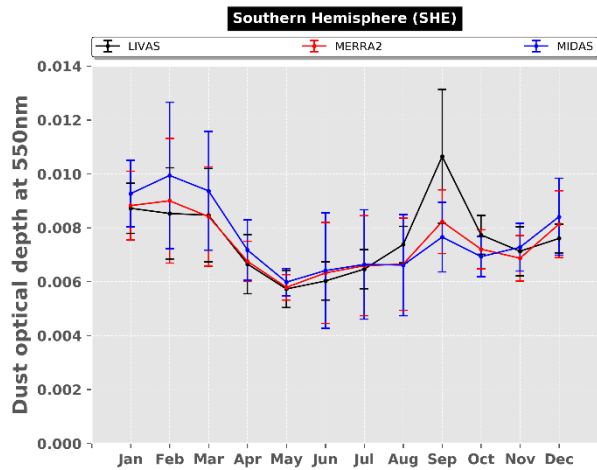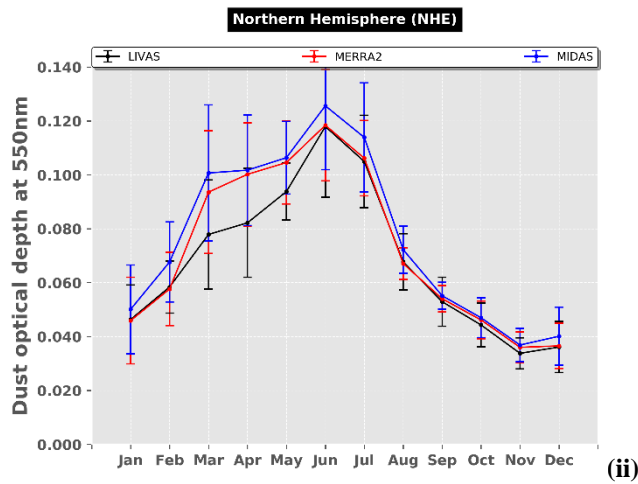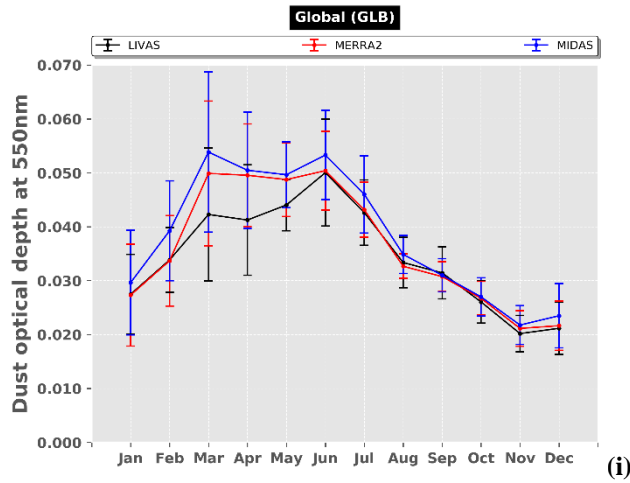
Figure 6: Monthly variability of LIVAS (black curve), MERRA-2 (red curve) and MIDAS (blue curve) DODs, regionally averaged over: **(i)** the whole globe (GLB), **(ii)** the Northern Hemisphere (NHE) and **(iii)** the Southern Hemisphere (SHE). The error bars correspond to the monthly interannual standard deviation computed during the period 2007 – 2015.

1736

Figure 7: Regional domains of: East Tropical Atlantic (**ETA**), West Tropical Atlantic (**WTA**), Mediterranean (**MED**), Gulf of Guinea (**GOG**), West Sahara (**WSA**), Sub-Sahel (**SSA**), Bodélé Depression (**BOD**), North Middle East (**NME**), South Middle East (**SME**), Central Asia (**CAS**), Thar Desert (**THA**), Taklamakan Desert (**TAK**), Gobi Desert (**GOB**), East Asia (**EAS**), West North Pacific (**WNP**), East North Pacific (**ENP**) and Southwest United States (**SUS**).
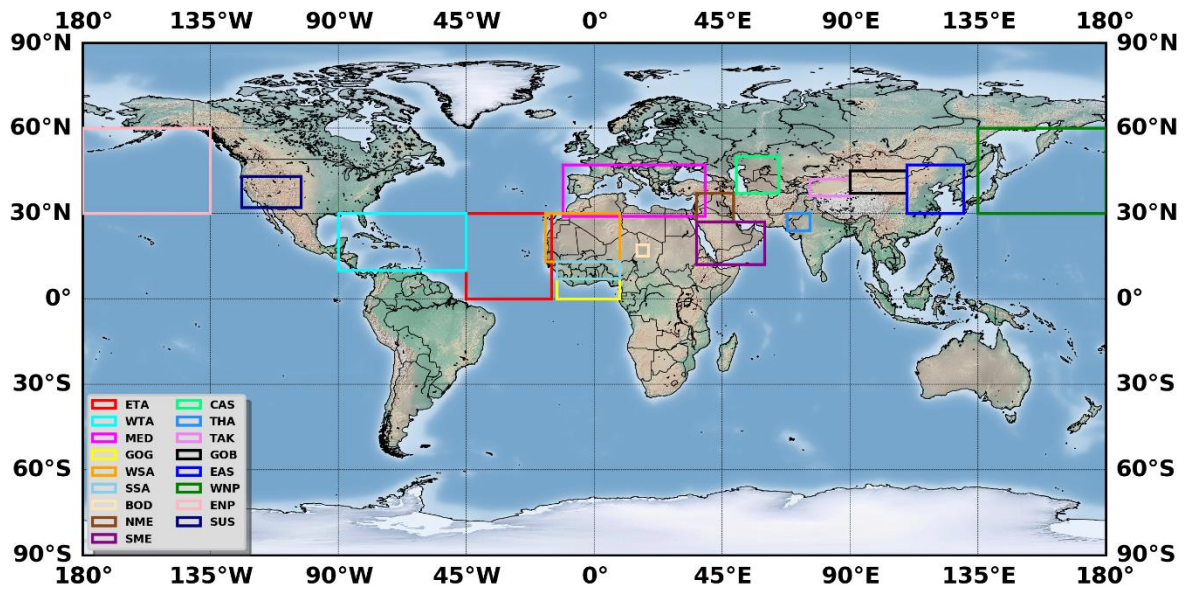
1741

1742

1743

1744

1745

1746

1747

1748

1749

1750

1751

1752

1753
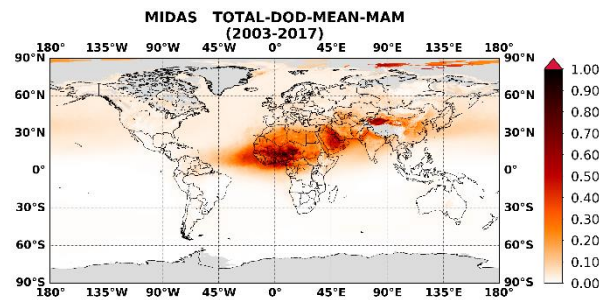
1754
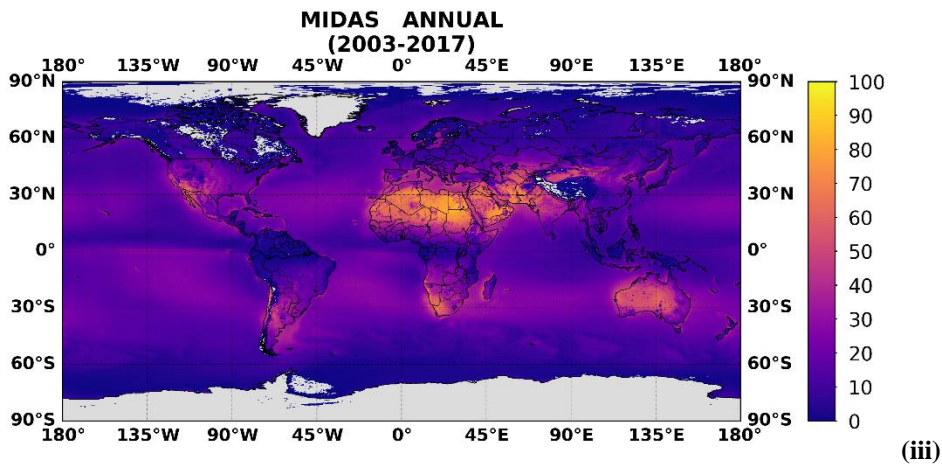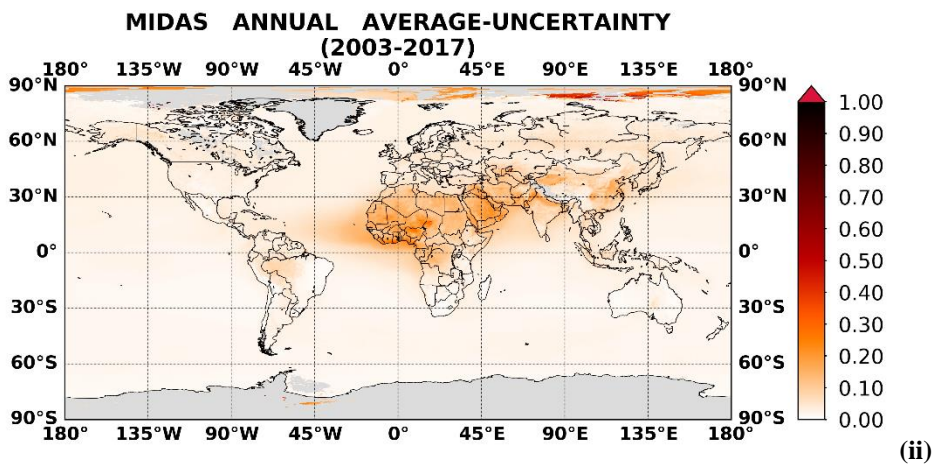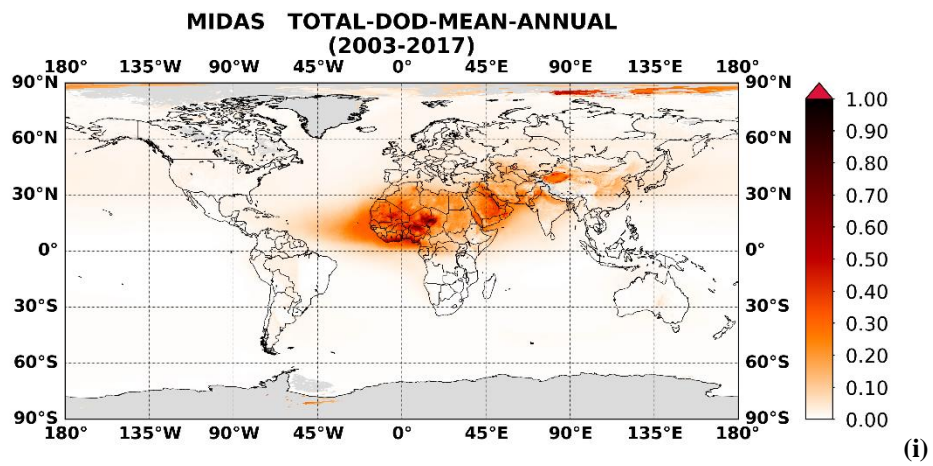
Figure 8: Annual geographical distributions, at 0.1° x 0.1° spatial resolution, of: **(i)** the climatological DODs, **(ii)** the average of the daily DOD uncertainties and **(iii)** the percentage availability of MIDAS data with respect to the entire study period spanning from 1 January 2003 to 31 December 2017. Grey color represent areas with absence of data.
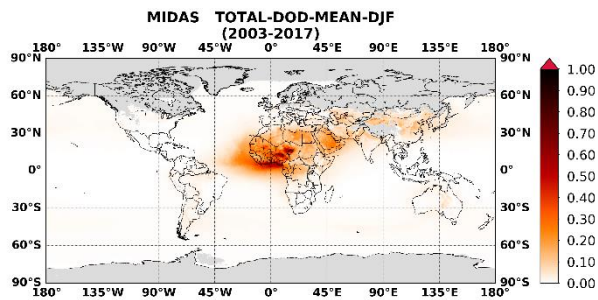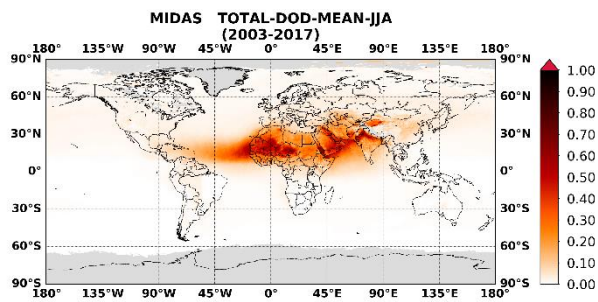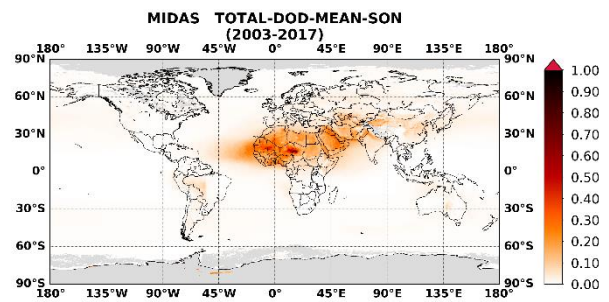
Figure 9: As in Figure 8-i but for: **(i)** December-January-February (DJF), **(ii)** March-April-May (MAM), **(iii)** June-July-August (JJA) and **(iv)** September-October-November (SON).